

Review

Visualizing vasculature and its response to therapy in the tumor microenvironment

Qiaoya Lin, Peter L. Choyke, Noriko Sato✉

Molecular Imaging Branch, Center for Cancer Research, National Cancer Institute, National Institutes of Health, Bethesda, Maryland.

✉ Corresponding author: Noriko Sato, MD, PhD. Molecular Imaging Branch, Center for Cancer Research, National Cancer Institute, National Institutes of Health, Bethesda, MD 20892. Phone: 1+240-858-3079; Fax: 1+240-541-4526; Email: saton@mail.nih.gov.

© The author(s). This is an open access article distributed under the terms of the Creative Commons Attribution License (<https://creativecommons.org/licenses/by/4.0/>). See <http://ivyspring.com/terms> for full terms and conditions.

Received: 2023.04.04; Accepted: 2023.07.30; Published: 2023.09.25

Abstract

Tumor vasculature plays a critical role in the progression and metastasis of tumors, antitumor immunity, drug delivery, and resistance to therapies. The morphological and functional changes of tumor vasculature in response to therapy take place in a spatiotemporal-dependent manner, which can be predictive of treatment outcomes. Dynamic monitoring of intratumor vasculature contributes to an improved understanding of the mechanisms of action of specific therapies or reasons for treatment failure, leading to therapy optimization. There is a rich history of methods used to image the vasculature. This review describes recent advances in imaging technologies to visualize the tumor vasculature, with a focus on enhanced intravital imaging techniques and tumor window models. We summarize new insights on spatial-temporal vascular responses to various therapies, including changes in vascular perfusion and permeability and immune–vascular crosstalk, obtained from intravital imaging. Finally, we briefly discuss the clinical applications of intravital imaging techniques.

Keywords: intravital imaging, tumor vasculature, optical imaging, animal window models, vascular responses

Introduction

Tumor vasculature differs from normal vasculature in morphology, structure, and function, and plays a critical role in tumor progression and metastasis [1], drug delivery [2], resistance to therapies [3], and antitumor immunity [4]. In contrast to the normal blood vessels (Figure 1A), the tumor vasculature is strikingly heterogeneous and highly disorganized, lacking the hierarchy of vessel diameter (e.g. arterioles, capillaries, and venules) observed in normal tissues, as depicted in Figure 1B [5]. In normal tissues, the endothelial barrier consists of two types of intercellular junctions: adherens junctions and tight junctions (Figure 1C). However, in tumor vessels, there are defective endothelial junctions with larger gaps between endothelial cells (Figure 1D), abnormal pericytes [6], and a lack of smooth muscles or basal membrane. The impaired endothelial barrier structure [7] creates a tumor microenvironment (TME) characterized by leaky vasculature and impaired blood flow, which result in hypoxia, low pH, and high

interstitial fluid pressure.

The endothelial barrier in the TME is a dynamic structure that controls the exchange of fluids and solutes, as well as various cells. Extravasation of cells and drugs occur via one of two types of mechanisms: paracellular and transcellular pathways (Figure 2) [9]. Paracellular pathways are generated by gap junctions, where cells are initially slowed during transit but then migrate through the gap junction. The enhanced permeability and retention (EPR) effect, commonly associated with tumors has been a central paradigm for drug delivery since the late 1980s [10], however, the magnitude of the EPR effect in human tumors is often very small. EPR is related to inherent vascular leakage, poor lymphatic drainage, and slower blood flow in tumors, all of which favor the passage of macromolecules through paracellular inter-endothelial gaps, enhancing their passive diffusion and accumulation in the tumor. Recently, the contribution of the EPR effect to drug extravasation has been

challenged by the discovery of transcellular extravasation as the primary route of transport for certain nanoparticles, such as gold nanoparticles (Figure 2)

[11]. Transcellular extravasation is mediated by endothelial vesicles that actively transports solutes across the endothelial cell, even against a gradient.

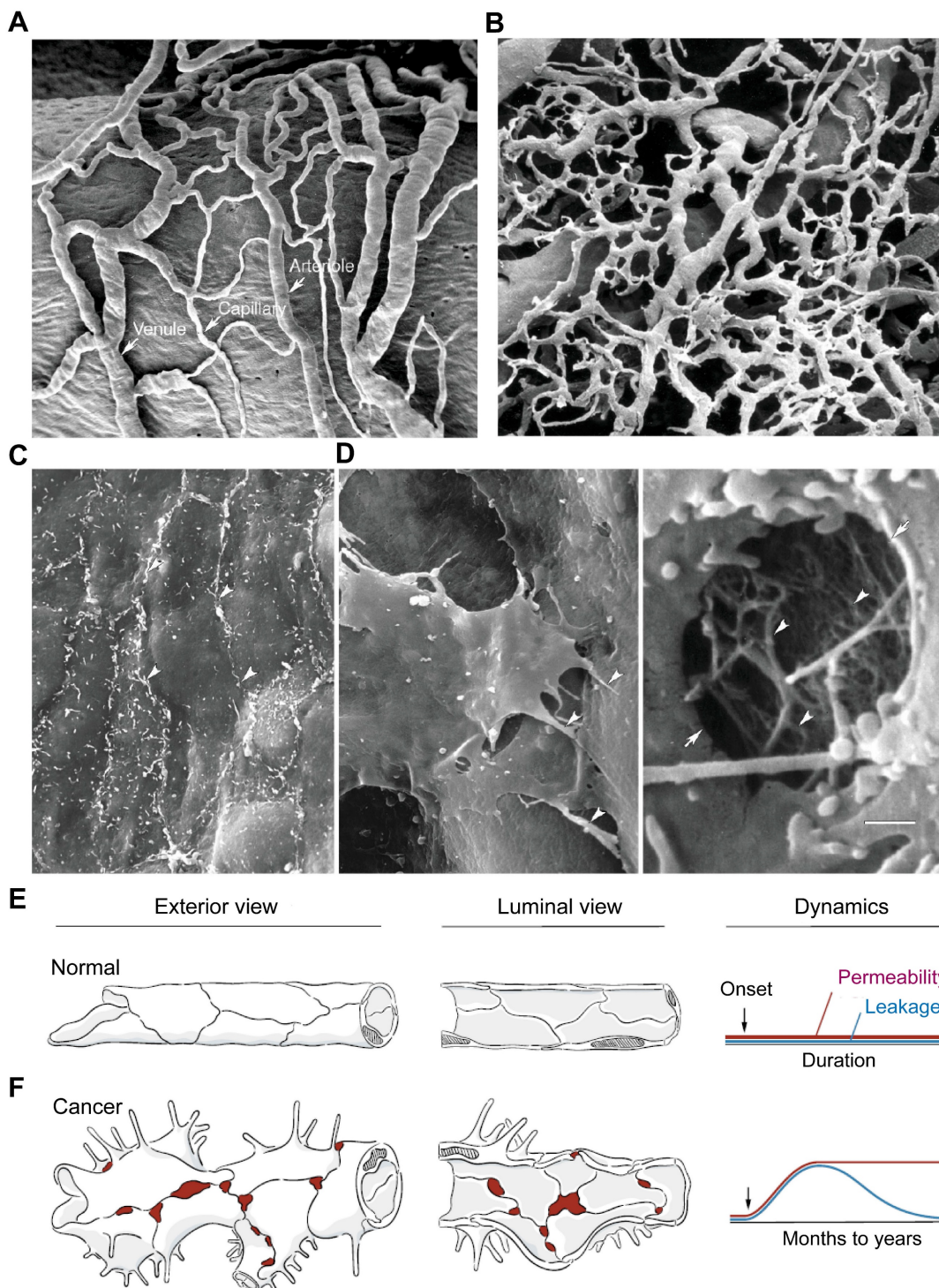


Figure 1. Tumor vasculature are morphologically, structurally, and functionally abnormal. (A) Scanning electron microscopic (SEM) imaging of normal microvasculature (vasa vasorum of rat carotid sinus) polymer cast shows an organized arrangement of arterioles, capillaries, and venules. (B) SEM image of a tumor microvasculature cast demonstrates disorganized vessels without the conventional hierarchy (i.e., arterioles, capillaries, and venules). A and B are adapted from [5, 8] with permission, copyright 2003 Springer Nature and Dr. Lametschwandner. (C) SEM image of the luminal surface of normal blood vessel, which is smooth and has tight endothelial junctions (arrowheads, mouse mammary gland). (D) SEM of a tumor vessel shows widened intercellular spaces, overlapping endothelial cells, multiple cellular processes, and other abnormalities (left, arrowheads, MCalV mouse mammary carcinoma). High magnification of a hole in the endothelium (arrows) shows the underlying basement membrane filaments (right, arrowheads). Scale bar in D applies to panels A-D (50 μ m in A and B; 5 μ m in C; 2 μ m in D left; 0.5 μ m in D right). Adapted from [5, 8] with permission, copyright 2003 Springer Nature. (E, F) Comparison of exterior and luminal views of blood vessels of the microcirculation and corresponding dynamics of permeability and leakage over time under normal conditions (E) and in cancer (F). In normal blood vessels, the permeability and leakage are low and stable. In cancer, increased endothelial permeability is sustained, but leakage decreases as interstitial pressure rises because of impaired lymphatic drainage. Modified from [7] with permission, copyright 2021 Elsevier.

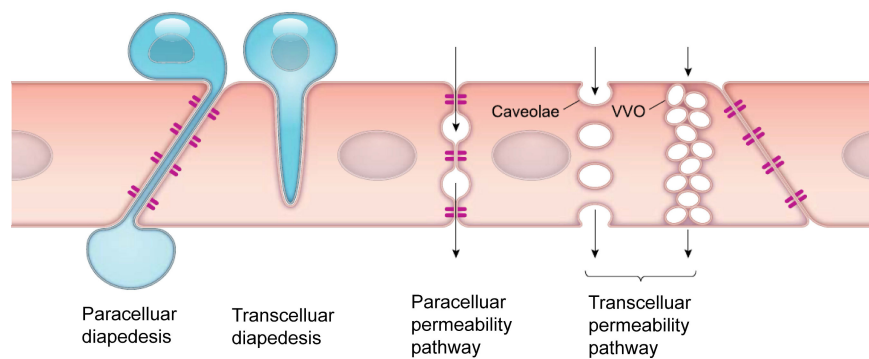


Figure 2. Transendothelial pathways for cells and solutes. Cells such as leukocytes can pass through the endothelial cell layer by paracellular and transcellular diapedesis. Endothelial permeability for macromolecules can be increased by opening endothelial junctions or through activation of vesicle-based transcellular pathways. VVO: vesiculo-vacuolar organelle. Modified from [9] with permission, copyright 2019 The American Physiological Society.

Table 1. Tumor vasculature spatiotemporal measurements.

Chamber-based animal model	Diameter (μm)	Intercellular; Intracellular openings (μm)	Permeability ($\times 10^7$ cm/sec)	Ref
U87 mouse cranial window		0.07-0.1; ND	3.8 \pm 1.2 (2.4–5.0)	[18]
HCa-1/ST-8 mouse dorsal chamber		0.38–0.55/0.55-0.78; ND	2.06 \pm 1.44 (1.60–3.99)/3.73 \pm 3.34 (1.67–9.28)	[18]
LS174T mouse dorsal chamber		0.4-0.6/0.38-0.55; ND	1.24 \pm 0.45 (0.56–1.67)	[18]
MCa-IV mouse dorsal chamber		1.7 \pm 0.1; 0.6 \pm 0.1	2.5 \pm 1.5 (1.2–5.1)	[19]
P22 rat dorsal chamber	13(6-35)			[20]
Xenograft/orthotopic mouse model	Diameter (μm)	Vessel sprout length (μm)		Ref
RIP-Tag2 pancreatic islet tumors	8 \pm 1(5-16)	15 \pm 1(3-56)		[21]
Lewis lung carcinomas	31 \pm 2(5-154)	23 \pm 4(5-56)		[21]
MCa-IV mammary Carcinomas	45 \pm 6(8-294)	29 \pm 4(3-69)		[19, 21]
Renal clear cell carcinoma, asalioma	6-55	2-52(Intervascular); 34-208(Interbranching)		[8]
Sarcomas, colon carcinoma	5-80	11-105(Intervascular); 11-160(Interbranching)		[8]

Footnotes: ND: no data

Abnormal tumor vasculature can also impede the transport and/or distribution of drugs, oxygen, and the infiltration of immune cells, such as T cells. As a result, abnormal tumor vasculature can contribute to resistance of tumor cells to chemotherapy, radiation therapy, and immunotherapy [12]. Additionally, tumor endothelial cells can release several hypoxia-related factors such as vascular endothelial growth factor A (VEGF-A), which induces the expression of programmed cell death protein 1 (PD-1), T-cell immunoglobulin mucin-3 (TIM-3), and cytotoxic T-lymphocyte-associated protein 4 (CTLA-4) on CD8 T cells, rendering them dysfunctional. Alongside prostaglandin E2 (PGE2) and interleukin (IL)-10, VEGF-A induces Fas ligand (FasL) expression on endothelial cells, that affects the survival of effector T cells (rather than regulatory T cells (Tregs)). The expression of Clever-1/stabilin-1 on tumor vascular endothelial cells and hypoxia-related chemokine CCL-28 further aid the preferential recruitment of Tregs. Moreover, the hypoxic TME recruits monocytes that give rise to myeloid-derived suppressor cells (MDSCs) and tumor-associated macrophages (TAMs) and induces a differentially and functionally immature phenotype of DCs, collectively supporting an immunosuppressive TME. The more glycolytic metabolism of tumors results in acidification of the TME, thereby inhibiting

cytotoxicity activities of CD8 T cells [4, 13-16].

Due to the critical roles of tumor vasculature in defining the TME, monitoring morphological and functional changes of the vasculature in response to therapies holds significant importance. Imaging techniques of vessels need to match both spatial and temporal scales to dynamically assess the tumor vasculature. As summarized in Table 1, in order to obtain sufficient spatial information, the method must be flexible enough to capture both the full extent of vessel sprouting (hundreds of millimeter resolution) as well as identify intercellular openings in tumors vasculatures (~70 nanometer resolution). Higher scanning speeds or temporal resolutions provide greater information for imaging changes in dynamic permeability. Functional imaging allows for assessment of perfusion, immune-vascular crosstalk (including immunocytes, cytokines, and vessel interactions) and oxygen saturation, all of which are equally important as structural analysis [7, 8, 17]. Vascular imaging techniques should also possess the ability to record various functional events *in vivo* at multiscales [9]. In this review, we describe recent advances in intravital tumor vascular imaging, covering imaging of vessels within tumors in live animals and humans. Focus will be put on *in vivo* real-time optical imaging technologies utilizing intravital microscopy (IVM) and animal window

models. Clinical applications of these technologies are also discussed.

Methods to Visualize Vasculature *In Vivo*

Brief history of *in vivo* tumor vascular imaging

In the past several decades, various imaging techniques, including computed tomography (CT), positron emission tomography (PET), magnetic resonance imaging (MRI), and ultrasound, have been developed and utilized to visualize tumor vasculature at different scales, both in preclinical and clinical settings. Previous reviews have covered the use of these modalities for imaging angiogenesis at different scales [5]. With the evolution of those technologies, the spatial resolution of blood vessel imaging has dramatically increased. For instance, CT resolution has progressed from approximately 500 μm using CT angiography to 100 μm for microcomputed tomography (micro-CT), 50 μm for volumetric computed tomography [22], and even down to 400 nm for nano-computed tomography (nano-CT) (Figure 3). Current clinical and small animal PET

scanners have a spatial resolution of approximately 1.5 mm–5 mm (Figure 3). MRI has the advantage of using magnetic fields rather than potentially harmful ionizing radiation for visualization. The spatial resolution of MRI has improved from hundreds of micrometers to 10 micrometers with micro-MRI [5] (Figure 3). Ultrasound, which does not involve ionizing radiation, is also commonly used to visualize vasculature. The resolution of conventional clinical ultrasound imaging is 200 μm –1 mm due to fundamental diffraction limits (Figure 3). Super-high resolution ultrasound with ultrafast frame rates (more than 500 frames per second), achieving resolutions of around 1 μm , has been developed [23, 24].

Advances in intravital tumor vascular imaging

In recent years, development and improvements in optical imaging methods have facilitated improved imaging of the tumor vasculature *in vivo*. These methods offer higher resolution, deeper imaging depth, and greater metabolic information. With these techniques, it is now possible to image the heterogeneous tumor blood vessels at the single-cell level,

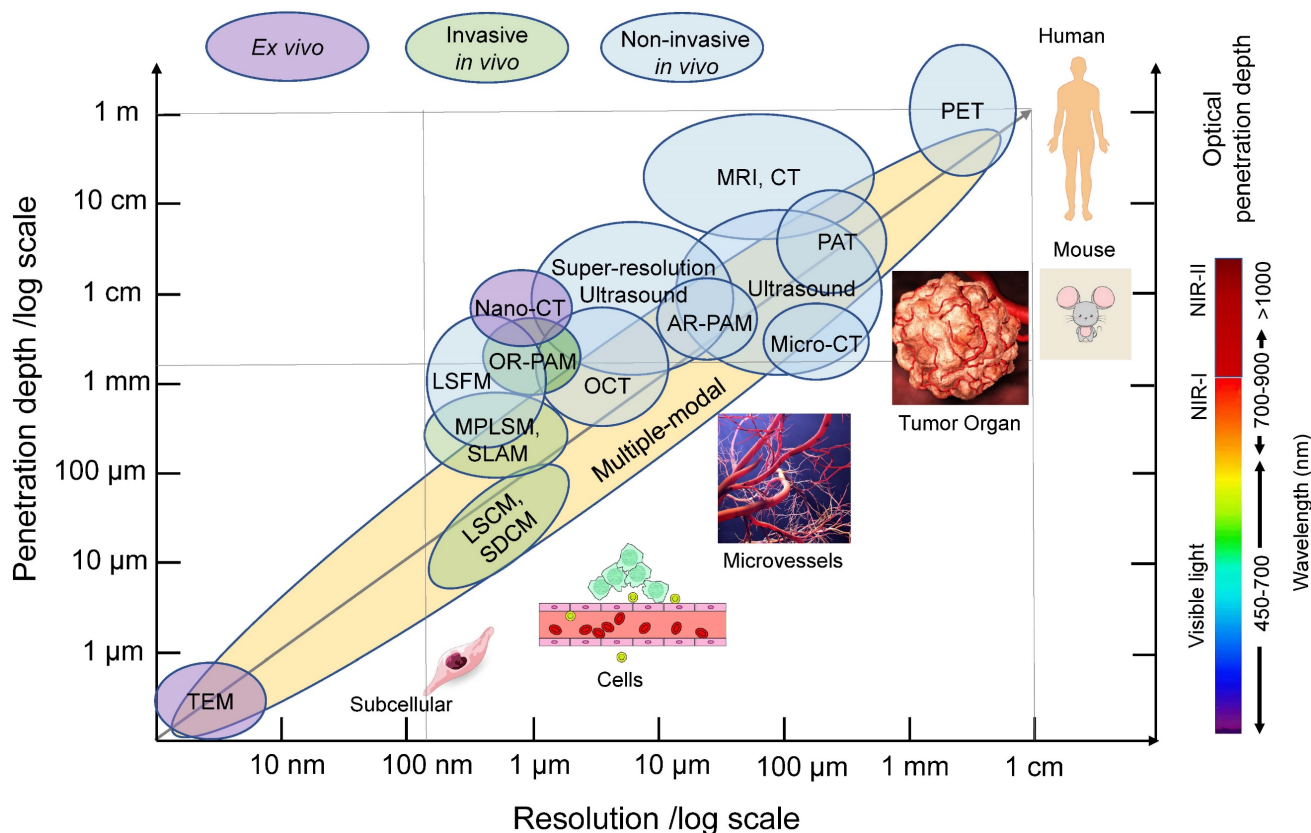


Figure 3. Common *in vivo* tumor vascular imaging techniques and their resolution and penetration depth. Non-invasive (blue circles) and invasive (green circles) *in vivo* imaging techniques and *ex vivo* imaging techniques (purple circles) for vascular imaging are shown in relation to their resolution and tissue penetration depth. Multi-modality imaging (yellow) takes advantage of combining techniques. The optical penetration depth increases as the wavelength increases from visible light, NIR-I to NIR-II. PAT: photoacoustic tomography, AR-PAM: acoustic-resolution photoacoustic microscopy, OCT: optical coherence tomography, LSFM: light-sheet fluorescence microscopy, OR-PAM: optical-resolution photoacoustic microscopy, MPLSM: multiphoton laser scanning microscopy, SLAM: simultaneous label-free autofluorescence-multiphoton microscopy, LSCM: laser scanning confocal microscopy, SDCM: spinning disk confocal microscopy, TEM: Transmission electron microscopy, NIR: near-infrared.

even without the need for labeling. Additionally, dynamic changes within the vasculature can be recorded, providing valuable information on cell-to-cell interactions using multi-color imaging. This section focuses on highlighting the most recent advances in intravital tumor vascular imaging techniques, primarily intravital microscopy (IVM) methods, as depicted in Figure 4. Additionally, new animal window models will be discussed, which have contributed to these advancements.

IVM: Confocal microscopy and multiphoton laser scanning microscopy

The most commonly used methods in intravital imaging are confocal microscopy, including laser scanning confocal microscopy (LSCM) and spinning disk confocal microscopy (SDCM), as well as multiphoton laser scanning microscopy (MPLSM). Compared to wide-field fluorescence microscopy, LSCM addresses some of the scattering effects of fluorescent light by incorporating a pinhole aperture at the confocal plane in front of the detector, which rejects fluorescence from other planes (Figure 4A, left panel) [25]. The spatial resolution can reach ~200 nm

in the lateral dimension and ~500 nm in the axial dimension at ~30 frame per second (fps) scanning speed (Figure 3). This high-resolution enables visualization of fine tumor vessels *in vivo*. However, this imaging technique has a limited imaging depth (<~100 μm) and relatively high photobleaching and phototoxicity, leading to time limited imaging and/or tissue damage.

MPLSM utilizes the simultaneous nonlinear absorption of two-photons or three-photons generated by femtosecond pulsed lasers, to excite fluorophores [26] in the near-infrared (NIR) region (Figure 4D). MPLSM provides better tissue penetration and less scattering, thus providing advantages for three-dimensional and deep-tissue imaging ($\geq 500 \mu\text{m}$) [27, 28] (Figure 3). Moreover, MPLSM can provide metabolic information by imaging autofluorescence of nicotinamide dinucleotide (NADH) and flavin adenine dinucleotide (FAD) using endogenous fluorophores. Additionally, MPLSM allows label-free imaging by collecting second-harmonic generation (SHG) signals [29], which occur at highly ordered non-centrosymmetric structures, such as, fibrillar collagen in the TME. Third

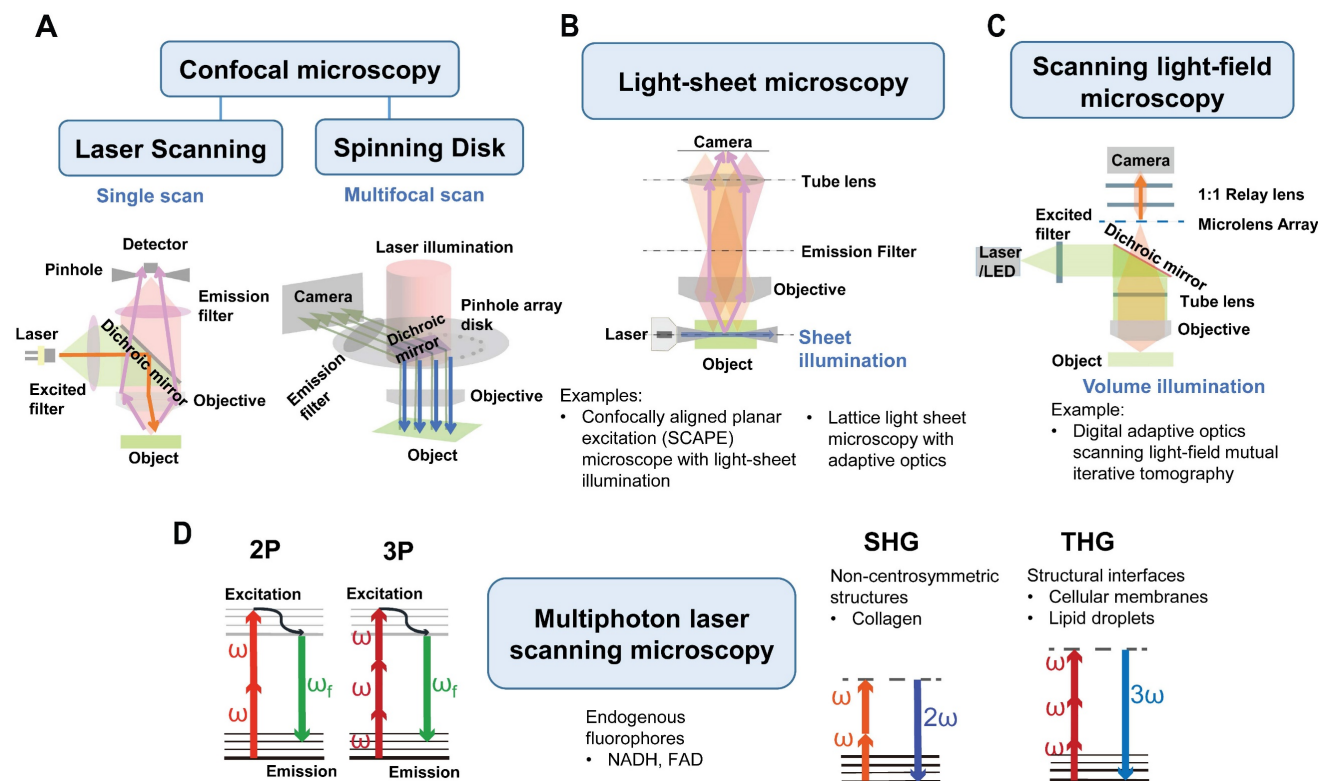


Figure 4. IVM methods in tumor vascular imaging. Current microscopies used in intravital tumor vascular imaging: (A) Confocal microscopy: laser scanning confocal microscopy (single scan type) and spinning disk confocal microscopy (multifocal scan type), (B) Light-sheet microscopy (sheet illumination or plane illumination), (C) Scanning light-field microscopy (volume illumination) and (D) Multiphoton laser scanning microscopy (MPLSM). (A-C) Schematic diagram of those microscopies. In (A-C), a fluorophore is excited by absorbing one single photon of a certain wavelength. (D) In MPLSM, the fluorophore is excited by simultaneously absorbing two photons (2P) or three photons (3P) of a longer wavelength. MPLSM can provide metabolic information by imaging endogenous fluorophores of nicotinamide dinucleotide (NADH) and flavin adenine dinucleotide (FAD). MPLSM allows label-free imaging by collecting second-harmonic generation (SHG) and third-harmonic generation (THG) signals. The SHG occurs at highly ordered non-centrosymmetric structures, such as fibrillar collagen, whereas the THG occurs at structural interfaces, such as cellular membranes and lipid droplets.

harmonic generation (THG) microscopy is also employed to image cellular membranes, lipid droplets [30] and collagen bundles or muscle fibers [31]. THG occurs at structural interfaces, such as the third-order nonlinear susceptibility χ^3 . Unlike SHG, THG does not require a specific asymmetric structure to be imaged and is usually elicited by water-lipid and water-protein interfaces. It causes a tripling of the frequency of the excitation wavelength, whereby the combined energy of three photons is converted into one emitted photon with one-third of the excitation wavelength but triple the energy [32]. Thus, THG has demonstrated excellent potential for label-free intravital imaging.

MPLSM was first used in *in vivo* imaging and quantification of tumor angiogenesis in 2001 by Brown EB *et al.* [33]. Since then, multiphoton microscopy has been widely utilized in tumor vascular imaging [20, 34]. A recent development in this field is simultaneous label-free autofluorescence-multiharmonic (SLAM) microscopy, developed by You S *et al.* It features fast epi-detection of NADH from three-photon autofluorescence (3PAF) and FAD from two-photon autofluorescence (2PAF), combined with non-centrosymmetric structures from SHG and tissue interface features from THG in a single-excitation source nonlinear imaging platform (with a custom-designed excitation window at 1110 nm and shaped ultrafast pulses at 10 MHz) (Figure 5A) [35]. By using SLAM microscopy, they visualized the leukocyte recruitment cascade without labeling in a rat mammary tumor model. Two modes of leukocyte arrest in the tumor vasculature, slow rolling (Figure 5B) and immediate arrest (Figure 5C), were detected. Another two-photon phosphorescence lifetime microscopy (2PLM) can measure the oxygen partial pressure (PO_2) and blood flow using specific molecular probes [36, 37]. A recent study further demonstrated the strength of MPLSM for stain-free histopathology by integrating 2PAF, 3PAF, SHG, THG and coherent anti-Stokes Raman scattering (CARS) or stimulated Raman scattering (SRS), enabling the detection of a variety of vital events in carcinogenesis including tumor cell migration and angiogenesis [38].

Motion artifacts induced by heartbeats and respiration in the live animal are significant challenges to intravital imaging. One solution is to increase the scanning rate, then collect only those images obtained between the movements, a method of retroactive gating. The SDCM [39] has an opaque disk with hundreds of pinholes arranged in spirals that rotates at high speeds with extremely high scanning speed and low photodamage (up to ~1000

fps) (Figure 4A, right panel) [40]. Therefore, it is a valuable tool for recording rapid live events without motion-derived artifacts. Another solution is to correct the drift during or post imaging. A real-time tissue-drift correction system using graphics processing unit (GPU) computing, that can correct specimen drift along all axes at a speed of 150 ms per stack during scanning on the 2PE has been developed [41]. A new open-source software tool Galene can correct small movements in images collected by fluorescence lifetime imaging microscopy (FLIM) that require long acquisition times [42]. Recently, adaptive optics, a technology that improves the image quality of fluorescence microscopy by correcting sample-induced optical aberrations, has been developed with promising results [43].

Simultaneous acquisition of tumor vessel structure and function is important for determining the metabolic state in the TME. In addition to obtaining information on NADH/FAD via 2PE/3PE, IVM methods can determine glucose uptake, mitochondrial membrane potential (MMP), and oxygen saturation (sO_2) in cancer implants *in vivo* using fluorescence contrast agent 2- [N-(7-nitrobenz-2-oxa-1, 3-dioxol-4-yl) amino]-2-deoxyglucose (2-NBDG), tetramethyl-rhodamine ethyl ester (TMRE), and differential absorption spectra of oxygenated and deoxygenated hemoglobin, respectively [44]. In metastatic 4T1 mouse breast cancers, increased glucose uptake was observed across all sO_2 levels, indicating the "Warburg effect", and showed increased MMP relative to normal tissue. The 4T1 peritumoral areas showed a significant glycolytic shift relative to the tumor regions. In contrast, non-metastatic 67NR and 4T07 mouse breast cancers displayed increased MMP but comparable glucose uptake relative to normal tissue.

No single imaging technique can visualize tumor blood vessels at multiscale (Table 1), and this has led to the development of multimodal imaging based on several intravital imaging techniques. Karreman MA *et al.* proposed a multimodal correlative approach combining IVM, micro-CT, and three-dimensional (3D)-electron microscopy (EM) (Figure 6). They captured single tumor cells (JIMT1 GFP-labeled HER2-positive human breast cancer) in the vasculature (labeled with 500 kDa TRITC-dextran) of the cerebral cortex and subcutaneous tumors, providing unique insights into metastatic events. With this method, accurate (<5 μ m) correlation of functional imaging to the ultrastructural analysis of single cells is possible in a relevant microenvironment [45].

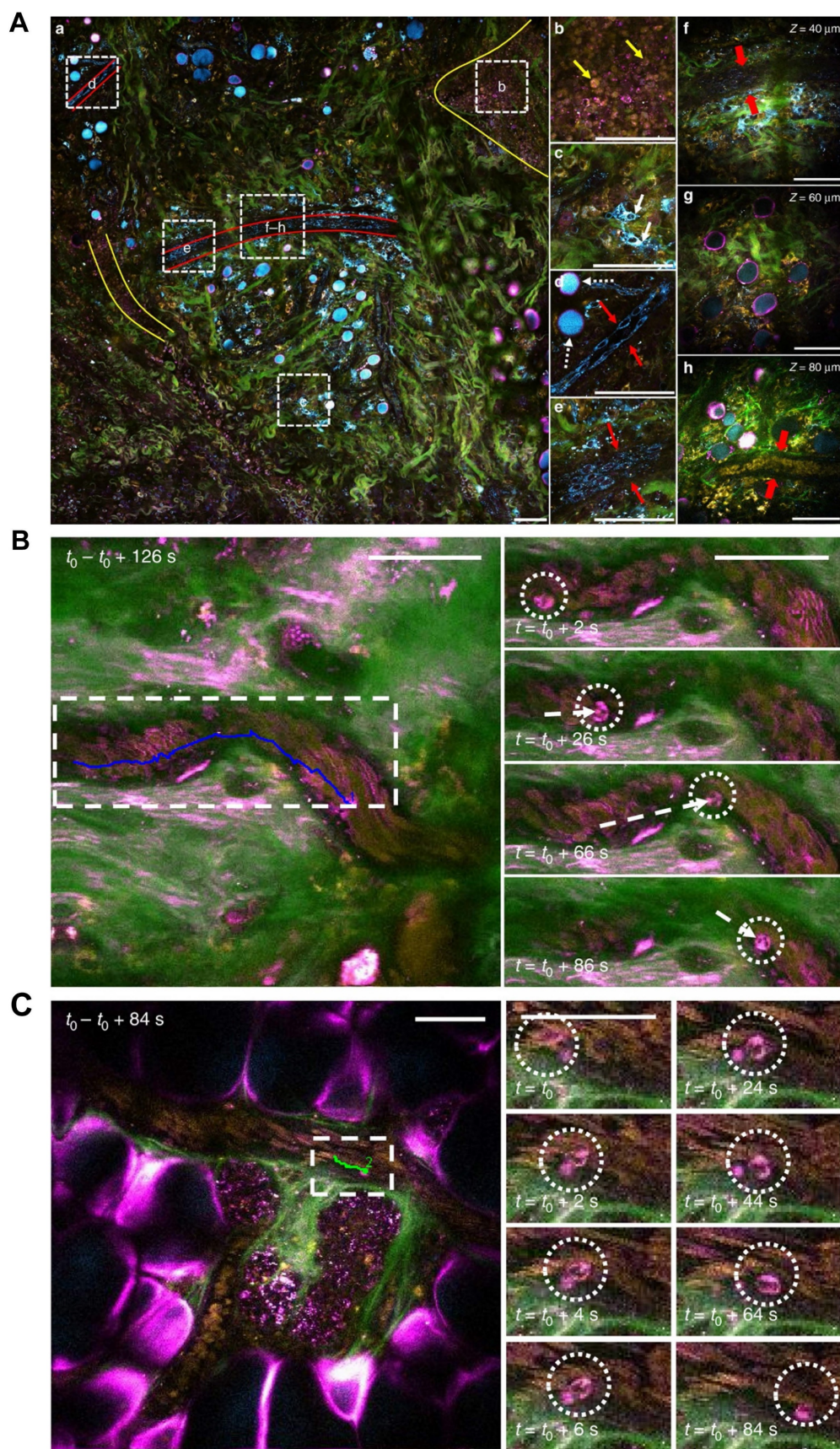


Figure 5. *In vivo* label-free multi-color tumor vascular imaging. (A) Tumor microenvironment of a live rat by SLAM microscopy. A full large field of view (1.5×1.5 mm²) at the N-Nitroso-N-methylurea induced mammary tumor boundary is shown (A-a), with different regions of interest (white dashed squares) magnified in b-g. Tumor cell clusters and vasculature are highlighted with yellow and red boundaries, respectively. Green: SHG (collagen fibers), magenta: THG (interface), yellow: 2PAF (FAD), cyan: 3PAF (NADH). (A)-b Tumor cells (10 μm, yellow arrows) with co-localized 2PAF (FAD) and THG (interface) signals. (A)-c Larger (>20 μm) cells (white arrows) with strong 3PAF

(NADH) signals, which are likely to be macrophages based on their irregular cell shape and oval-shaped nucleus. **(A-d, e)** Vascular endothelial cells (red arrows) and adipocytes with THG-strong boundaries and NADH-strong content inside (white dashed arrows). **(A-f-h)** Images acquired from different depths, showing a hollow vessel composed of a layer of endothelial cells, without red blood cells (f), and a mature vessel filled with red blood cells (h, contrast is enhanced to show blood cells in deeper layers). Scale bar: 100 μm . **(B, C)**. Two modes of leukocyte arrest captured by SLAM microscopy. A multi-nucleated neutrophil slowly rolling along the vessel wall **(B)** and immediate arrest of a leukocyte with a sudden halt in the movement, followed by adhesion and crawling **(C)**. Scale bar: 50 μm . Modified from [35] with permission, 2018 Springer Nature.

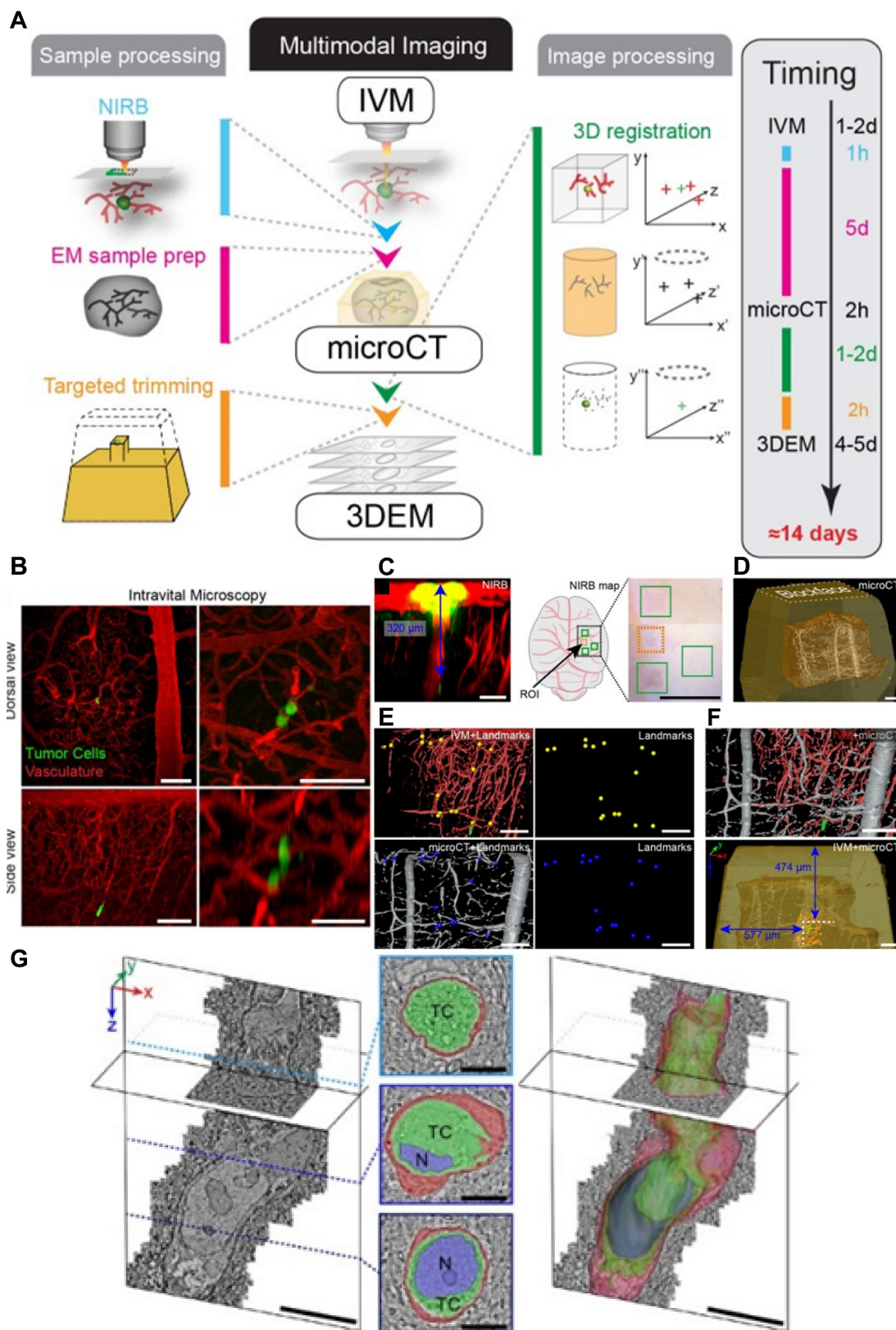


Figure 6. Multimodal vascular imaging combining IVM, micro-CT, and 3D-EM. (A). Workflow for multimodal correlative microscopy. First, the event of interest is captured with IVM (1-2 days), and an ROI is marked with the tissue surface with near-infrared branding (NIRB) (1 hour). A biopsy containing the ROI is dissected and resin-embedded for EM analysis (1+4 days), and then imaged with micro-CT (2 hours). The IVM imaged volume is registered to the micro-CT volume using Amira software (1-

2 days), which allows determination of the position of the resin-embedded ROI relative to the surface of the block. The resin block is trimmed to expose the tumor cell for EM imaging (2 hours). Finally, 3D-EM of the ROI is performed (4–5 days). **(B–F)**. IVM and micro-CT imaging of tumor cells in the mouse brain cortex blood capillary after intracardiac injection of the cells, followed by 3D registration. **(B)**. IVM analysis of an arrested tumor cell (green) in the brain cortex vasculature (red). Dorsal views (z-projection, large field of view, top panels) and side views (x, z-projection, small field of view, bottom panels) of the ROI, 2 days (left panels) and 3 days (right panels) post tumor cell injection. Scale bars: 100 μm in left panels, 50 μm in right panels. **(C)**. After IVM acquisition and perfusion fixation, the ROI is marked with NIRB on the brain surface, producing autofluorescence (yellow) in both the green and red channels. The x, z projection (left) shows the distance (blue arrow) between the tumor cell (green, lower in the panel) and the NIRB landmark at the surface. A cartoon and an image of the mouse brain show the NIRB landmark (orange box) positioned above the ROI and three additional reference marks (green boxes) created to facilitate targeting of the ROI when dissecting the biopsies. Scale bars: 100 μm (left panels), 1 mm (right panels). **(D)**. The micro-CT shows the tissue biopsy (brown) within the resin block (yellow) and the vessels (gray). Scale bar: 100 μm . **(E)**. 3D registration of the vasculature as segmented from the IVM (top) and micro-CT (bottom). Corresponding points are marked in the IVM (yellow spheres) and micro-CT (blue spheres) volumes. Scale bars: 100 μm . **(F)**. Based on the marks generated in **E**, the IVM volume is registered into the micro-CT data with Amira software (top), enabling precise determination of the tumor cell (green) position within the resin block and relative to its surface (bottom). Scale bars: 100 μm . **(G)**. Focused ion beam scanning EM imaging of a tumor cell arrested in the vasculature (z-stack, 6350 frames, 8 nm isotropic voxel size). Image frames were segmented to show the tumor cell (TC, green), its nucleus (N, blue) and the capillary's endothelial cells and basal lamina (red). Scale bars: 10 μm (3D models), 5 μm (segmented sections). (Modified from [45] with permission 2016 Company of Biologists Ltd).

IVM: Light-sheet fluorescence microscopy and scanning light-field microscopy

In addition to laser scanning confocal microscopy, MPLSM, and SDCM, light-sheet fluorescence microscopy (LSFM) [46] is emerging as a promising tool for imaging tumor vessels. LSFM uses a thin sheet of light to excite only fluorophores within the focal plane (Figure 4B). As such, LSFM has a true optical sectioning capability and, hence, provides excellent axial resolution while minimizing the photobleaching and phototoxicity to a fraction of the sample. The average spatial resolution is ~ 230 nm in the lateral dimension and ~ 450 – 600 nm in the axial dimension. LSFM is commonly used for long-term 3D observations of live biological specimens such as *Caenorhabditis elegans* and zebrafish [47]. Voleti V *et al.* developed an improved swept, confocally aligned planar excitation (SCAPE) microscope with light-sheet illumination that can achieve high-resolution volumetric imaging at over 300 volumes per second with over 1.2 GHz pixel rates. They successfully analyzed real-time blood flow and calcium dynamics in the beating heart of transgenic zebrafish expressing enhanced green fluorescent protein (EGFP) in endothelial cells and DsRed in red blood cells (RBCs) (Tg(flk1:EGFP)s843; Tg(gata1:DsRed)sd2) [48]. LSFM has been combined with tissue-clearing techniques for 3D organ imaging. Applications include exploring tumor tissue complexity [49], the brain microvasculature and routes of glioblastoma cell invasion [50] and heterogeneity of macrophage infiltration and therapeutic response in lung carcinoma [51]. LSFM has been recently reviewed [52].

Modifications to LSFM have further improved its utility. Liu TL *et al.* combined non-invasive lattice light-sheet microscopy with aberration-correcting adaptive optics to study a variety of delicate subcellular events *in vivo*, including organelle remodeling during mitosis. Various tumor cell motions within blood vessels of zebrafish embryos have also been studied: tumor cells exhibit rolling while extending long, adhesive microvilli and crawling while conforming to the shape of a vessel,

and, finally, transendothelial extravasation (Figure 7A–C) [53]. However, this technique is applicable only to a small field of view imaging, and tiling the corrective adaptive optics restricts overall speed over a large volume.

Long-term, high-speed imaging at subcellular resolution and low photon doses remains a challenge in mammals. To overcome these barriers, Wu J *et al.* proposed a computational imaging framework, termed digital adaptive optics scanning light-field mutual iterative tomography (DAOSLIMIT) [54]. It features high-speed, high-resolution 3D imaging, tiled wavefront correction, and low phototoxicity. In contrast to LSFM which tomographically scans through the volume, plane by plane, light-field microscopy acquires the entire volume simultaneously using an extended depth of field (Figure 4C). Volumetric imaging of $225 \times 225 \times 16 \mu\text{m}^3$, with a resolution of up to 220 nm laterally and 400 nm axially, is obtained at the millisecond scale resulting in hundreds of thousands of data points. With DAOSLIMIT, Wu J *et al.* studied the dynamics of cancer cell migration by injecting human breast cancer cells expressing PH-mCherry into the vasculature of zebrafish expressing EGFP in endothelial cells [Tg(fli:eGFP)] [54]. Vasodilation occurs as a cancer cell approaches a vessel turn, followed by vasoconstriction as the cell floats away (Figure 7D). Notably, some cancer cells are trapped in small-bore microvessels, and large internal vesicles can be seen to split and be released under the stress of intravascular flow (Figure 7E–F). These observations raise some interesting possibilities: while cancer cells may reduce their cell-body volume to escape from small-bore microvessels, these “splitting vesicles” may deliver signals to distant organs promoting further metastases. Similarly, circulating tumor cells-derived microparticles have been reported to migrate along the lung vasculature and are mainly taken up by interstitial myeloid cells, contributing to metastatic seeding [55]. Another interesting observation is the generation of retraction fibers and migrasome-like vesicle structures when multicellular clumps of cells are retained in vessels (Figures 7G–H).

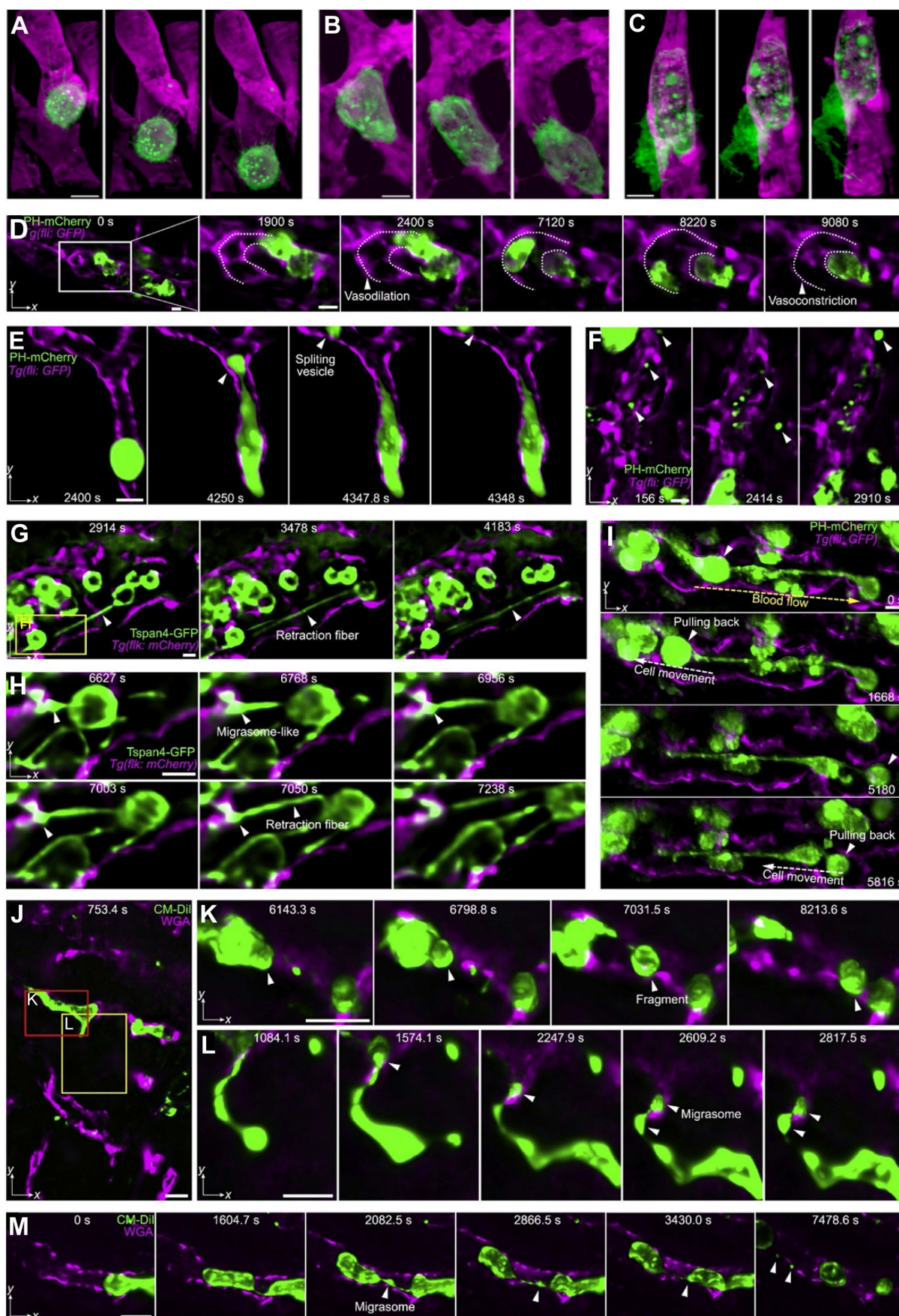


Figure 7. Subcellular intravital imaging of tumor cell migration and membrane dynamics in zebrafish and mouse models. (A–C). MDA-MB-231 human breast cancer cells (mCherry-CAAX, green) were intravenously injected into a transgenic zebrafish embryo 48 hpf (endothelial cell kdrl: gfp, magenta). The cells are observed rolling

in a vessel (A) or crawling along the endothelium (B). A cancer cell in transendothelial migration shows an increasingly complex morphology over time (C). Scale bars, 10 μm . Adapted from [53] with permission 2018 The American Association for the Advancement of Science. (D-I) MDA-MB-231 cells injected pericardially into blood vessels of a transgenic zebrafish larvae [Tg (fli: GFP), magenta] are observed. (D) Maximum intensity projections show vasodilation as a cancer cell (PH-mCherry, green) approaches a turn in the vessel and vasoconstriction is seen as the cell exits the field of view (dashed lines: vessel contour). (E) A tumor cell splits a large vesicle (arrowhead) when trapped in a small-bore vessel. (F) Various vesicles are observed flowing in the vessels. (G and H) Cancer cells (Tspan4-GFP, green) generate retraction fibers and migrasome-like vesicles when dissociating from multicellular clumps under flow shear stress. (I) Cancer cells (PH-mCherry, arrowheads) are pulled back by retraction fibers even against the blood flow. The direction of blood flow (yellow dashed arrow) and that of cell movement (white dashed arrow) are indicated. (J-M) HeLa human cervical cancer cells (membrane dye CM-Dil, green) migrate in mouse liver vasculatures following a splenic injection. The vessels are labeled by intravenously injected AF647-wheat germ agglutinin (magenta). HeLa cells split off large fragments when trapped in the small vessels (K) and generate retraction fibers and migrasomes during migration (L and M). Scale bar, 10 μm . Adapted from [54] with permission, 2021 Elsevier.

Long-term imaging showed that some of the escaping circulating tumor cells were pulled back to the multicellular clumps by retraction fibers even against strong blood flow (Figure 7I), which suggests that retraction fibers help maintain circulating tumor cells as clusters. The investigators found similar phenomena in mammals as well. HeLa cells trapped in small vessels demonstrated split large vesicles and cell fragments within mouse livers (Figure 7J-K) and also generate retraction fibers and migrasomes during migrations along the vasculature (Figures 7L-M). These observations reveal unexpected and complex behaviors of circulating cancer cells and highlight the importance of DAOSLIMIT for understanding this process more thoroughly.

IVM in the second near-infrared window

Light scattering by biologic tissues limits the penetration of light depth in tissues of live mammals *in vivo*. A practical approach to reduce light scattering and increase imaging depth is to extend the excitation and emission wavelengths to the second near-infrared window (NIR-II: >1,000 nm). The NIR spectrum region is divided into three channels: NIR-I (700-900 nm), NIR-IIa (1,300-1,400 nm), and NIR-IIb (1,500-1,700 nm) channels. Visualizing tumor vasculatures via a NIR-II imaging system relies on a NIR-II contrast agent. In the past 15 years, NIR-II contrast agents have significantly advanced [56]. Examples include, inorganic single-walled carbon nanotubes (SWNTs) [57, 58], quantum dots [59], rare-earth doped down-conversion nanoparticles [60], and organic NIR-II molecules or protein complex [61, 62], such as aggregation-induced emission (AIE) luminogens (AIEgens) [63].

Wide-field fluorescence imaging in the NIR-II window combined with one or more of those contrast agents can achieve 1~4 mm of imaging depth but remains limited in resolution. Various NIR-II microscopies have been developed recently with high-resolution and/or 3D mapping capability. NIR-II spinning-disc confocal microscopy [64], has a lateral resolution of $0.5 \pm 0.1 \mu\text{m}$ and an axial resolution of $0.6 \pm 0.1 \mu\text{m}$. NIR-II light-sheet microscopy (LSM) with excitation and emission of up to approximately 1,320 nm and 1,700 nm, respectively, has a penetration depth of up to 750 μm , lateral

resolution of 0.9-1.6 μm and an axial resolution of 2.6-4.4 μm . In addition to imaging tumor microcirculation with NIR-II LSM, 3D molecular imaging of immune checkpoint proteins has been performed at the cellular scale in live animals [65]. This imaging system was extended to structured-illumination light-sheet microscopy (NIR-II SIM) with excitation and emission wavelengths in the NIR-IIb window [66]. The integration of structured-illumination into NIR-II light-sheet microscopy diminished out-of-focus background, improving the spatial resolution by 1.7 times and facilitating long-term *in vivo* imaging of cell behavior in intact tissues without surgery. Moreover, this team also developed superconducting nanowires with single-photon counting detectors and quantum dots for longer than 1,700 nm to conduct confocal fluorescence microscopy in intact rodents [67].

Quantification of hemodynamics using IVM

In addition to the development of microscopy, advanced quantitative methodologies for measuring blood flow in tissues, including tumors, is important. Kamoun WS *et al.* developed two MPLSM-based methods to simultaneously quantify blood flow (i.e., velocity, flux, hematocrit, and shear rate) in complicated blood vessel networks at single-capillary resolution *in vivo* [68]. One is called residence timeline scanning (RTLs), which allows direct flow velocity analysis by scanning the line at an arbitrary angle to the vessel. The other is relative velocity field scanning (RVFS), which is a full-field method that allows simultaneous analysis of most vessels in a field of view by deconvolving the image distortion produced by the moving cells relative to the moving laser scans. Honkura N *et al.* developed a time-lapse intravital imaging-based image analysis tool, RVDM (relative velocity, direction, and morphology), to monitor rapid changes in specific types of vessels [69]. RVDM relies on the laser scan speed, relative velocity, and direction of blood flow, to produce parametric images of RBCs in vessels. It allows the identification of vessel categories by their RBC velocity dynamics. By using RVDM in transgenic mice expressing GFP in the endothelial cells under a tight junction marker Claudin5 (Cldn5) promoter [Cldn5(BAC)-GFP], they revealed that capillaries and postcapillary venules in

normal mouse skin, with no or low *Cldn5* expression, respond to VEGFA with rapid changes in blood flow, vessel tone, and leakage. This approach could also be used in distinguishing heterogeneous tumor vessels in future.

Hypoxia in solid tumors can be a limiting factor for therapeutic efficacy. Hypoxic heterogeneity is considered to arise from abnormal tumor vasculature, but the precise mechanisms are not well understood. Bernabeu MO *et al.* introduced a metric to characterize tumor vasculature (mean vessel length-to-diameter ratio, λ) and demonstrated how it predicts tissue-oxygen heterogeneity, based on MPLSM imaging [70]. RBC transport plays a role in establishing oxygen heterogeneity in tumor tissue, and λ could be used to monitor the efficacy of antiangiogenic agents and provide a proxy measure of perfusion and oxygenation in the tumor. Moreover, Enjalbert R *et al.* proposed a computational model to investigate the impact of vessel compression on RBC dynamics in tumor vascular networks [71]. Vessel compression alters RBC partitioning at bifurcations in a hematocrit-dependent and flow rate-independent manner. These findings contribute to hemodilution and partitioning of RBCs within tumor vascular networks resulting in regional hypoxia that may be reversible following pharmacological decompression.

Other techniques: Photoacoustic imaging

Photoacoustic imaging (PAI) is a non-invasive imaging technique that utilizes non-ionizing laser pulses to induce ultrasound pulses that can be detected with an ultrasound transducer. The light pulse absorption by molecules in tissues creates a thermal pressure wave that propagates ultrasonic waves, which are detectable with ultrasound transducers (light in-sound out). In conventional ultrasound, the sound is produced at the transducer, and the reflected sound is detected again at the transducer (sound in-sound out). There are three major types of PAI based on resolution and image depth: optical-resolution photoacoustic microscopy (OR-PAM, resolution: 0.2-10 μm , depth: 1-2 mm), acoustic-resolution photoacoustic microscopy (AR-PAM, resolution: 15-50 μm , depth: 3-10 mm) and photoacoustic computed tomography (PAT, resolution: 100-500 μm , depth: 10-100 mm) [72]. Therefore, PAI encompasses a range of spatial resolution that at one end can detect organelles while at the other end can image whole animals or humans [73, 74] (Figure 3). PAI has developed rapidly in the last decades, with innovations such as fast PAI [75], high-throughput PAI [76], deep blood oxygenation imaging (in whole tissue) [77] and multi-modal imaging (photoacoustic and SDCM or 2P and SHG microscopy) *in vivo* [78, 79].

Optical absorption reflects endogenous total hemoglobin concentration ($\text{THb} = \text{Hb} + \text{HbO}_2$) and oxygen saturation ($\text{sO}_2 = \text{HbO}_2 / \text{THb}$), making PAI a useful tool to monitor vasculature changes, such as diameter, density, and tortuosity, in early tumors and oxygen saturation. Regional hypoxia can be demonstrated within solid tumors using *Thb* and blood sO_2 PAI. This has been confirmed in several tumor models, such as melanoma metastasis in brain [80] and xenograft and orthotopic breast cancer models [81, 82]. In general, *Thb* tends to be lower in the tumor core than in the periphery, consistent with poor central perfusion and high oxygen consumption. By changing the gas delivery to the mouse from room air to 100% oxygen (i.e., oxygen challenge) and measuring the induced change in sO_2 , an index of perfusion can be established [83, 84]. For example, a gas challenge on mice bearing subcutaneous PC3 or LNCaP human prostate cancers demonstrated smaller responding areas in the former tumor than the latter, with a high disparity between rim (rapid change) and core (no dynamic response), consistent with *ex vivo* findings of hypoxic and necrotic core tissues surrounded by a well perfused vasculature rim.

Methods to enhance signal-to-noise ratios in PAI have been explored. Genetic engineering of cells to express photoacoustic contrast is an attractive method to selectively label cells of interest to study their biological behaviors *in vivo*. For instance, cells transduced with a tyrosinase produce an absorbing pigment eumelanin that creates a strong photoacoustic contrast. Tyrosinase-expressing human tumor xenograft is detectable at nearly 10 mm depth with a spatial resolution below 100 μm in mice, enabling documentation of their growth and surrounding vasculatures [85]. Silver (Ag) nanoplates also have the potential as a PAI contrast agent with strong absorption for quantitative image-based evaluation of tumor vasculature and heterogeneity after intravenous infusion [86].

Other techniques: Optical coherence tomography

Optical coherence tomography (OCT) has made great strides in the last 30 years [87]. OCT is a non-invasive, interferometry-based technique that generates cross-sectional images of tissue by detecting the back-scattered photons with NIR low-coherence light [88]. Similar to ultrasound imaging in which sound pulse reflections (echoes) are measured to create an image, OCT uses the low coherence properties of a broadband light source, and light reflections which are measured with a Michelson interferometer. OCT is commonly used as a label-free technique that enables anatomical and physiological imaging of tumor blood vessels. Compared with IVM,

OCT has deeper tissue penetration (2-3 mm), a wider field of view, and higher imaging speed, but suffers from lower resolution ($<10\ \mu\text{m}$) (Figure 3). Vascular OCT imaging has been widely used in both preclinical and clinical studies [89, 90]. It has been employed to visualize blood vessels in human malignant melanoma and normal skin [91], identify specific tumor vasculature subtypes in human choroidal osteoma [92], and observe vasculature response to vascular-targeted photodynamic therapy [93] and photoimmunotherapy [94]. Research advances in vascular OCT imaging have been reviewed elsewhere [95, 96]. Multimodal OCT addresses the limitations of OCT by combining it with other imaging modalities. For instance, in a study using an orthotopic melanoma model, murine tumor capillaries were visualized at various resolutions, and vessel density quantification was compared across different modalities, including MRI, PET, CT, ultrasound, OCT, and high-resolution episcopic microscopy [97].

Recent advances in animal window models

In addition to the imaging techniques discussed above, achieving clear visualization of tumor vasculature at high resolution relies on the selection of animal window models and their technical advancements.

Animal window models and surgical preparation

Since the early intravital imaging of lymph nodes 20 years ago [98, 99], various rodent window techniques have been introduced to visualize blood vessels, from the superficial skin to internal organs (Supporting Table 1). The dorsal window chamber (DSWC) is created by stretching skin tissue over a ring, whereupon a tumor cell injection or tumor tissue implantation is performed on the dorsal skin in order to observe subcutaneous tumor progression and vasculature changes [100]. Smaller and lighter DSWC minimize animal burden [101, 102]. Another type of superficial window model is the mammary fat pad-based window models (MWCs), primarily utilized for visualizing the blood vessels in orthotopic breast cancer models or studying the metastasis behavior of tumor cells [103]. These windows are typically installed once the tumor has formed. Both DSWCs and MWCs are compatible with MRI and other imaging modalities [104, 105]. Furthermore, a recent development involves a flexible and sutureless silicon window that enables visualization of muscle tissue and orthotopic breast cancer [106]. Bone windows have been created for imaging brain tumor vasculature [107] and bone marrow [108, 109]. The cranial window [107] is mainly used for cerebral vessel imaging while the femur window [110, 111] is

used for bone marrow imaging. Either method can be used for tracking single cell extravasation as well as visualizing both tumor and endothelial dynamics over a long time period. The cranial window to visualize tumor blood vessels in the brain utilizes either thinned skull transcranial windows, reinforced thinned skull windows, transcranial windows, implanted windows or implanted prism, or lens windows [112]. Cranial windows can be used in combination with other imaging modalities, for example, ultrasonography and MPLSM/OCT [113], MRI, MPLSM and CT [114], and MPLSM and PET [112] imaging.

Imaging internal organs, especially within the thoracic or abdominal cavities, poses significant challenges due to their inaccessibility and the continuous motion of these organs. To enable high-resolution imaging of blood vessels in the lungs, several vacuum-stabilized lung windows have been developed. These windows can be used for extended periods, typically lasting several hours [115, 116]. Additionally, a long-term murine lung window has been introduced, allowing for the visualization of cancer metastasis through the blood vessels over a span of several weeks [117]. Similarly, intravital vascular imaging in the liver involves both simple non-survival models (that can last 6 hours [118, 119]) and longitudinal observation models (4-5 weeks) that utilize titanium abdominal windows [120] (Supporting Table 1). These abdominal window techniques are applicable to imaging other organs, such as the spleen, kidney, intestines, and pancreas [120, 121]. For example, they have been used to observe insulin secretion from pancreatic tail [122], and to characterize abnormal tumor blood vessels in various pancreatic cancers, including spontaneous transgenic tumors and orthotopically inoculated cancers, by comparing them to the normal pancreatic vasculature [123]. Abdominal windows are also compatible with multiple-modality imaging, such as combining MPLSM with laser speckles imaging, or MPLSM with MRI [122, 123]. Furthermore, the use of window models has been extended to evaluate the normal reproductive system, including the ovary [124] as well as recently implanted embryos [125].

Labeling methods

Visualization of vessels mostly relies on some form of blood vessel tagging. Two types of vessel detection methods are used in intravital vascular imaging: One uses transgenic animals, in which endothelial cells exhibit a specific fluorescent signal. For example, in the endothelial nitric oxide synthase transgenic (eNOS)tag-GFP mice [102], GFP positive cells represent the endothelial cells, while in the

VeCad-tdTomato transgenic mice [117], TdTomato fluorescence protein is expressed in the endothelial cells. Another approach is to use exogenous labeling such as a dye conjugated to albumin that has large molecular mass to remain intravascular. Such agents can be intravenously injected, enhancing the blood vessel. Alternatively, a dye-conjugated antibody specific for an endothelial cell marker can be infused to tag the endothelial cells lining the vessels. Dextran with various molecular weights (10, 50, 70, 155, or 2000 kDa) are used to evaluate different vascular functions and leakiness of vessels. A direct infusion of a dye DiI has been used to enhance the vessels against the background [126]. For antibody labeling, CD31, VCAM-I and P-selectin are often used as endothelial cell biomarkers (Supporting Table 1, also reviewed in [5, 127, 128]).

Tumor Vascular Responses to Therapy

Visualization of morphological and functional changes in tumor vasculature in response to therapies can offer valuable insights into the effects and mechanism of these treatments, ultimately contributing to improved treatment outcomes. This section describes intravital imaging findings of dynamic vascular responses to different therapies and discusses new insights implicating an immune-vascular crosstalk observed in various therapies.

Chemotherapy

Chemotherapy is a generic term for a family of cytotoxic anticancer therapies. *In vivo* image findings of drug delivery [129, 130] and drug effects [131-133] at single-cell resolution and imaging chemotherapy induced angiogenesis and "normalization" of tumor vasculatures has been reviewed extensively. Increased pericyte coverage, improved tumor vessel perfusion, reduced vascular permeability, and consequently reduced hypoxia, have been observed during tumor vascular normalization in which the neovasculature becomes more organized in response to therapy [34, 134, 135]. Here we highlight recent findings of chemotherapy-induced vascular permeability changes observed by IVM.

As described in the Introduction section, the extravasation of cells and drugs can occur through either the paracellular or transcellular pathway [9]. Investigations utilizing IVM have provided insights into the paracellular pathway of cell extravasation and the involvement of cells and cytokines in treatment-induced changes in permeability. For instance, in a spontaneous mouse model of breast cancer (MMTV-PyMT mice), IVM helped to demonstrate that doxorubicin treatment induces recruitment of myeloid cells expressing matrix

metalloproteinase 9 (MMP9) into the tumor via the CCL2/CCR2 chemokine/chemokine receptor axis. This recruitment correlated with the degree of vascular leakage, as detected using 10 kD dextran. Interestingly, in the absence of MMP9, vascular leakage increased due to enlarged endothelial gap junctions and decreased pericyte coverage, resulting in a better tumor response to doxorubicin treatment [136].

Harney *et al.* showed that the secretion of VEGFA by perivascular TIE2^{hi} macrophages led to a local transient increase in vascular permeability, known as "bursting," which facilitated intravasation of breast cancer cells through vessels with reduced pericyte coverage and junction integrity [137]. This finding supports the concept of the "tumor microenvironment of metastasis" (TMEM), which involves a perivascular TAM contacting with a mammalian-enabled (MENA)-overexpressing tumor cell and endothelial cell, creating a front for cancer cell intravasation [137]. Similarly, paclitaxel treatment increased the infiltration of perivascular TIE2^{hi}/VEGF^{hi} macrophages, induced TMEM-dependent transient and localized vascular permeability, and enhanced breast cancer metastasis. This observation correlated with high expression of MENA on the disseminating cancer cells [138]. Other common chemotherapy treatments, such as doxorubicin/cyclophosphamide treatment, showed similar pro-metastatic changes. Conversely, inhibition of the TIE2 receptor using rebastinib or knockdown of the MENA gene reversed chemotherapy induced TMEM activity and cancer cell dissemination [138].

Interestingly, another study demonstrated tumor vascular "bursting" in the presence or absence of leukocytes in the perivascular area [139]. In contrast to other studies that utilized dextran, this study used 30 nm or 70 nm nanoparticles to examine vascular permeability. It is possible that the nanoparticles themselves had effects on the endothelial barrier, leading to "bursting" even in the absence of perivascular leukocytes. Certain types of nanoparticles have been reported to induce endothelial leakiness by disrupting VE-cadherin-VE-cadherin homophilic interactions at the cell-cell interface, which can facilitate cancer cell intravasation and extravasation [140].

Additionally, increased tumor vessel permeability and drug delivery via the paracellular pathway have been achieved by intraperitoneal injection of a transforming growth factor β (TGF- β) inhibitor, which induces defects in pericyte coverage [141], or by using doxorubicin-containing MMP2-responsive nanoparticles that release an anti-platelet antibody, leading to local depletion of tumor-associated platelets adhering

to the vessel wall [142].

The transcellular pathway can also mediate changes in vascular permeability, influencing drug delivery. This active transcytosis can occur through caveolae or vesicula-vacuolar organelles (VVOs). Caveolin-1 is critical for caveolae formation and caveolae-mediated transport, while inflammatory mediators or VEGF can induce VVOs involved in the extravasation of macromolecules [9, 143]. For example, IVM and TEM have documented an active transcytosis-mediated enhancement of permeability as the primary route for transporting certain nanoparticles [11]. Interestingly, neither knocking out caveolin-1 (thus lacking caveolae) nor vessel normalization using a VEGFR-2 blocking monoclonal antibody (DC101) had an impact on this transcytosis-dependent enhanced drug delivery. Further investigations are required to better understand the fundamental mechanism of the transcytosis pathway.

One strategy to induce caveolae-mediated transcytosis is the cationization of drug formulation at the luminal endothelial cell surface. This mechanism has been utilized to improve tumor penetration of camptothecin (CPT). Conjugation of CPT to a newly designed membrane γ -glutamyl transpeptidase-activatable polymer led to enhanced treatment efficacy compared to CPT-11 alone [144]. Similarly, conjugation of the small drug 7-ethyl-10-hydroxycamptothecin (SN38) to a poly(2-(N-oxide-N,N-diethylamino)ethyl methacrylate) (OPDEA)-based polymer facilitated tumor penetration via transcytosis. Treatment with this agent resulted in the eradication of tumor implants and patient-derived tumor xenografts in mice [145].

In contrast to the studies indicating improved drug delivery via permeability enhancement, several studies using acute myeloid leukemia (AML) models demonstrated that decreased vascular permeability benefited the treatment outcome. MPLSM functional imaging in a skull window model of AML engraftment indicated an association of AML with vascular abnormalities. The inability to restore normal vasculature following induction chemotherapy has been linked to a poor prognosis, likely attributed to excessive nitric oxide (NO) production. Importantly, inhibition of NO production improves treatment response to arabinosylcytosine *in vivo* [146]. A similar skull window model demonstrated that MMP inhibition reduced vascular permeability, suppressing AML infiltration and growth [147].

Other examples demonstrate the value of intravital microvascular imaging in understanding

the impact of therapies on tumor vasculature. For instance, fibroblast growth factor 9 was revealed to normalize tumor blood vessel structure for the vessel hierarchy and vasoreactivity, reducing tumor core hypoxia and VEGF-A expression [148]. Angiopoietin-4 increased vessel permeability by 4.5-fold and promoted lymphatic dilation and activation of TIE2-dependent signaling [149]. EphB4 overexpression resulted in resistance to sunitinib treatment in SF126 glioma subcutaneous and orthotopic models [150]. These chemotherapy-induced vascular permeability changes observed using IVM are summarized in Table 2.

Radiation therapy

The effects of radiation therapy (RT) on blood vessels highly depend on the radiation dose, timing, fraction size, as well as the type, location, and stage of the cancer [161-163]. Single, high-dose RT (> 10 Gy) has been shown to induce endothelial cell apoptosis [164, 165] by upregulation of ALK5 and sphingomyelinase [162], wherein vessels regress and blood flow decreases [166]. Eventually, new vessels are formed via the recruitment of endothelial progenitor cells and improvement of pericyte coverage of the vessel wall, a process thought to be mediated by the CXCL12/CXCR4 chemokines system and PDGF-B/PDGFR- β signaling [167, 168]. In contrast to high single-dose irradiation, fractionated low-dose irradiation exerts a proangiogenic effect on the vasculature by upregulating the NO pathway [169] and angiostimulatory growth factors, such as VEGF and placental growth factor, eventually inducing vascular growth and increased tissue perfusion [170].

A longitudinal investigation of human pancreatic tumor xenografts has been conducted to assess their response to different doses of RT (10, 20, and 30 Gy). This study utilized a swept-source OCT system in conjunction with a dorsal window chamber [171]. The findings revealed that immediately after irradiation, poorly vascularized and low-oxygen areas within the tumor increased, reaching their peak between 2-3 weeks post-irradiation. Subsequently, these areas returned to pre-irradiation levels in approximately 3 weeks. Compared to the unirradiated controls, this effect was more significant with doses of 30 Gy and 20 Gy, but not with 10 Gy irradiation. The study provides valuable insights into the temporal vascular response to different RT doses, which could contribute to predicting RT efficacy in future applications.

Table 2. Tumor blood vessel permeability response to different treatments.

Treatment	Permeability/ extravasation changes	Mechanism (cells, cytokines)	Ref
Angiopoietin-4	↑ 4.5-fold	Activation of TIE2-dependent signaling	[149]
Sunitinib	No change	EphB4 overexpression and treatment resistance	[150]
Doxorubicin	↑	MMP9-high myeloid cell recruitment via CCL2/CCR2. Possible VEGF↑ Loss of adherence junctions and decreased pericytes in MMP9 deficient mice	[136]
Paclitaxel, Doxorubicin/Cyclophosphamide	Transient ↑	TIE2 ^{hi} -TMEM macrophages, MENA↑	[138]
Nanoparticles (TiO ₂ , SiO ₂ , Au and Ag)	↑	Disruption of the VE-cadherin-VE-cadherin homophilic interactions at the adherens junctions	[140]
Nanoparticles (Polymers)	Transient↑	With or without leukocytes nearby	[139]
Nanoparticles (Au)	↑	Transcellular pathway; Active transcytosis	[11]
GGT activatable polymer-CPT conjugate nanoparticles	↑	Transcellular pathway: absorption-mediated transcytosis	[144]
SN38 conjugate polymer nanoparticle	↑	Transcellular pathway: absorption-mediated transcytosis	[145]
MMP2-responsive polymer-lipid-peptide nanoparticles delivering an antiplatelet antibody R300	↑	Local depletion of tumor-associated platelets that cover vessel wall	[142]
Inhibition of NO	↓	Restoring normal vasculature	[146]
MMPs broad-spectrum inhibitor prinomastat	↓		[147]
Low dose (5-Gy) radiation	Transient↑	TAM, NO signaling and VEGF	[151]
IFN γ (Overexpressed in tumor cell)	↓	Vascular density decrease (loss of smaller vessels and thinning of larger vessels)	[152]
TNF (Overexpressed in tumor cell)	↑	Vessels widening and burst	[152]
FGF-9 (Overexpressed in tumor cell)	n/a	A network of arterioles, bona fide capillaries, and venules; VEGF↓	[148, 153]
IL-1 β (2 μ g/ml)	↑		[154]
IL-1 β (1 μ g/ml)	-		
TGF- β inhibitor	↑	Fomation of pericytes in tumor vessels and reduce the solid pressure of tumors	[141]
PDT with photosensitizer MV6401	↑	Vasoconstriction; thrombus formation	[155]
Lower dose (0.25 to 0.5 mg/kg) verteporfin or EGFR-targeted nanobody-PDT	↑		[156]
PDT with verteporfin	↑	Endothelial cell microtubule depolymerization; endothelial intercellular gaps	[157]
RGD-modified ferritin-based PDT	↑	Larger fenestrae on the endothelial	[158]
PDT with the lipid- PLGA nanoparticles	↑	Tumor-associated myeloid cells	[159]
Tumor targeting PIT	↑		[160]

Footnote: FGF-9: fibroblast growth factor 9, EphB4: Ephrin type-B receptor 4, MMP9: matrix metalloproteinase 9, VEGFA: vascular endothelial growth factor A, TMEM: tumor microenvironment of metastasis, MENA: actin-regulatory protein mammalian-enabled, TiO₂: titanium dioxide, SiO₂: silicon dioxide, Au: gold, Ag: silver, VE-cadherin: vascular endothelial cadherin, GGT: γ -glutamyl transpeptidase, CPT: camptothecin, SN38: 7-ethyl-10-hydroxycamptothecin, NO: nitric oxide, IFN γ : interferon gamma, TNF: tumor necrosis factor, PDT: photodynamic therapy, EGFR: epidermal growth factor receptor, RGD: arginylglycylaspartic acid, PLGA: PEG layer coated poly (lactic-co-glycolic acid), PIT: photoimmunotherapy

Additionally, the effects of RT on tumor blood vessel permeability are time dependent. Shortly after irradiation, vascular permeability may increase because of the increased production of cytokines like VEGF. However, over time, vessel regression occurs, leading to reduced vascular permeability and a decrease in the total vascular surface area available for fluid and nutrient exchange [161]. Intravital imaging has proven valuable in elucidating RT-induced permeability changes and their underlying mechanisms. For example, using confocal microscopy in a dorsal window chamber with HT1080 human fibrosarcoma, a study examined the effects of a single low dose (5 Gy) irradiation. The findings revealed that irradiation induced a transient, dynamic, and localized vascular "bursting" phenomenon, leading to increased vessel volume, permeability, and tortuosity, thereby enhancing drug delivery [151]. Additionally, the study identified perivascular TAMs as being responsible for these vascular bursts and the subsequent enhanced drug delivery.

Immunotherapy

Cancer immunotherapy has revolutionized cancer treatment and was named the 2013

"Breakthrough of the Year" by the journal Science [172]. Immunotherapy is a broad category of therapy and includes therapies that use immune checkpoint inhibitors (ICIs), cytokines, adoptive cell transfer, targeted monoclonal antibodies, oncolytic viruses, and cancer vaccines [173-175]. This subsection illustrates recent intravital imaging observations in dynamic vascular responses to immunotherapy.

Programmed-death ligand 1 (PD-L1) is an immune checkpoint protein expressed by certain tumor cells that binds to programmed cell death protein 1 (PD-1) expressed on T cells, thereby inactivating T cells and evading immune surveillance. PD-L1 blocking antibodies, therefore, can activate the immune system and treat cancer [176]. Non-invasive *in vivo* 3D three-plex molecular imaging of a PD-L1-expressing CT26 mouse colon carcinoma was recently performed via NIR-II LSM [65]. In this study, the tumor cells, T cells, and vessels were labeled *in vivo* by intravenously injected Erbium-based rare-earth nanoparticles (ErNPs) conjugated to anti-PD-L1 antibody, PEGylated PbS/CdS core/shell quantum dot (CSQD) conjugated to anti-PD-1 antibody, and p-FE (comprised of organic dyes trapped in amphiphilic polymeric micelles approximately 12 nm

in size), respectively. PD-1⁺ T cells extravasating from vessels as well as surrounding PD-L1⁺ tumor cells were visualized, representing the first step in cancer cell-killing. This non-invasive imaging approach could be used in longitudinal studies to understand the mechanisms of therapy resistance. A possible way to overcome this problem has been reported based on an interesting observation in a dorsal window chamber model by Arlauckas SP and collaborators [177]. They tracked Alexa Fluor 647 conjugated anti-PD-1 antibody infused to label T cells in DPE-GFP/GREAT mice bearing MC38-H2B-mApple tumors. The anti-PD-1 antibody rapidly perfused tumor vessels spread into the tumor interstitium and bound to T cells as early as 5 minutes after injection. However, within minutes, the anti-PD-1 antibodies were transferred to neighboring PD-1 negative TAMs (labeled *in vivo* with phagocytosis of Pacific Blue-dextran nanoparticles) via Fc binding to the Fc-gamma (γ) receptors (Fc γ R) expressed on TAMs, compromising the efficacy of PD-1 therapy. *In vivo* blockade of Fc γ R before the anti-PD-1 antibody administration substantially improved the antibody binding to tumor-infiltrating CD8 T cells and enhanced therapeutic response.

The role of cytokines in immunotherapy response can be explored with IVM and tumor windows. Cytokines are soluble proteins that mediate cell-to-cell communication. Recombinant interferon (IFN) alpha (IFN- α) and interleukin (IL)-2 have been approved for the treatment of several malignancies [178]. Intravital imaging demonstrated that the cytokine effects on the tumor blood vessels are dose and time dependent. For example, IFN- γ was reported to induce regression of tumor vasculature between 24 and 96 hours after cytokine injection, resulting in the arrest of blood flow and subsequent collapse of tumors. In contrast, TNF was reported to dilate the blood vessels 24 hours after injection and induced a vascular “burst” at 36 hours [152]. In another study, administration of IL-1 β at a concentration of 2 μ g/ml, but not 1 μ g/ml, to mice bearing intracranial M6 glioma showed increased tumor blood vessel permeability [154].

Although promising, responses of cancer patients to immunotherapy are unpredictable and only a minority of patients respond to a single therapy. Therefore, combination therapies are being explored to improve patient outcomes. Combinations of immunotherapy with antiangiogenics, such as VEGF and angiopoietin 2, have been reviewed previously [179-182]. Another approach is to combine immunotherapy with RT. Longitudinal *in vivo* imaging and functional analysis revealed that 85% and 65% of T cells survive by fractionated IR (5 doses

of 1.8 Gy with 24 hour-intervals) and stereotactic body radiotherapy (SBRT, 20 Gy single dose), respectively, and show increased motility and higher production of IFN- γ compared with T cells from unirradiated tumors [183]. Intratumoral T cells in irradiated tumors appear to mediate tumor even without a fresh influx of unirradiated T cells. This study suggests new pathways for optimizing RT/immunotherapy combinations by uncovering a role for radiation-resistant intratumoral T cells. Moreover, RT facilitated rapid CAR T-cell extravasation and expansion within the tumor microenvironment, possibly due to increased vessel permeability, highlighting potential opportunities to improve adoptive T-cell therapy of GBM using concurrent RT [184]. Thus, combination immunotherapy shows some promise but the effects on the vessels can be difficult to predict.

Photodynamic therapy (PDT), photothermal therapy (PTT) and photoimmunotherapy (PIT)

Beyond immunotherapy, there are several other promising light-based anti-cancer therapies, such as photodynamic therapy (PDT), photothermal therapy (PTT), and photoimmunotherapy (PIT). We illustrate tumor blood vessel response to these photon-based therapies.

PDT is a treatment that uses a tumor-tropic photosensitizer that produces tissue-damaging cytotoxic reactive oxygen species upon exposure to light [185]. In the 1970s, PDT was first observed to induce vasoconstriction, occlusion, and platelet aggregation, leading to reduced tissue perfusion and hyperpermeability [185]. Furthermore, PDT increases vascular permeability due to the formation of endothelial intercellular gaps, which are likely induced by endothelial cell microtubule depolymerization and apoptosis [158]. IVM revealed that the effect of PDT on the vasculatures was dose dependent. For example, PDT using 1.0 mg/kg of photosensitizer verteporfin was more effective in inhibiting blood perfusion via thrombus formation, while a lower dose (0.25-0.5 mg/kg) verteporfin-PDT was more potent in enhancing dextran extravasation in an orthotopic R3327-MatLyLu rat prostate tumor model [156]. PDT also demonstrates vascular effects in a manner that depends on time after the treatment. In contrast to chemotherapy or immunotherapy, vascular effect of PDT showed similar changes when using different photosensitizers in various animal models. For example, PDT using the photosensitizer MV6401 showed biphasic blood flow changes with initial vasoconstriction in mouse mammary tumor (MCAIV) [155]. The acute responses were observed immediately after PDT, and

longer-term responses, such as thrombus formation, were observed more than 3 hours after PDT. Similarly, F8-small immunoprotein SIP mediated PDT induced microvascular stasis and thrombosis with reduced functional vessel density and perfusion in glioma, whereas total vessel density was not altered 24 hours after the treatment. The microvascular dysfunction recovered 4 days after treatment [186]. Acute vascular responses to PDT with an EGFR-targeted nanobody-photosensitizer have been evaluated by both intravital imaging using a skin-fold chamber model and dynamic contrast-enhanced MRI. Intravital imaging showed vasoconstriction and leakage in tumor and normal tissues in response to this nanobody PDT, and dynamic contrast-enhanced MRI confirmed a decrease in tumor perfusion [187]. Moreover, a recent high-resolution PAI with the ability to simultaneously record oxygenation images revealed that PDT might induce ischemia-reperfusion injury and provided an important insight into the mechanism of action of PDT. It showed that PDT with podeliporfin induced a substantial and immediate occlusion of the tumor vessels followed by hemorrhage within the tissue, and eventual collapse of the entire vasculature. Surprisingly, a temporal increase in oxygenation of the entire tumor volume was observed 5 mins after PDT, indicating rapid reperfusion from outside vessels, then dropped up to 24 hours [188].

Photothermal therapy (PTT) is another light-based noninvasive and selective treatment strategy for tumors. Unlike PDT that depends on production of reactive oxygen species, PTT functions via photothermal effects induced by converting light energy of near-infrared laser irradiation into heat [189]. Laser photocoagulation specifically affects the blood vessels surrounding and supplying nutrients and oxygen to the tumors and results in thermal destruction of the tumor tissue. The vascular disruption of VEGF-targeted photothermal therapy was monitored via intravital imaging in an orthotopic murine glioma model [190]. Vessel density increased by 18% for the saline group but decreased by 24% for the VEGF-NS treatment group over three days. A potential disadvantage of PTT is damage to surrounding normal tissues.

Photoimmunotherapy (PIT) is a cell-specific cancer therapy based on an armed antibody conjugated with a photosensitive dye that induces rapid and highly selective cancer cell necrosis and immunogenic cell death after NIR irradiation. Previous studies suggest that following PIT, there is a super-enhanced permeability and retention effect [160], which allows high concentrations of nanoparticles to accumulate in the tumor relative to pre-treatment permeability

levels. Real-time hemodynamic changes were monitored during PIT by OCT. It revealed that blood velocity in peripheral tumor vessels quickly drops while the vessel lumen enlarges. Ultraslow blood velocity could contribute to the long drug circulation time within the tumor, which could cause increased tumor blood pool volume [191].

Future Perspectives

Intravital imaging of tumor vasculature has made significant technical progress and provided a growing number of new insights in preclinical tumor models as discussed above. To enable more detailed investigation of tumor vasculatures and dissect underlying mechanism of biological events involving cells and vesicles, super-resolution intravital imaging that can reach 20-70 nm resolution is required. Such high-resolution imaging can, for example, visualize dynamic vesicle transport *in vivo* and help in understanding the mechanism and regulation of active transcytosis or transport through the endothelial gaps. The knowledge obtained from these fundamental studies would lead to improved cancer treatments.

Beyond the preclinical vascular studies, intravital imaging shows promise in visualizing tumor vessels in humans. Intravital imaging has been applied to the endoscopic evaluation of cancers in the gastrointestinal tract (such as in the esophagus [192, 193], stomach [194] and colon [195]), the cystoscopic evaluation of bladder urothelial cancer [196], the evaluation of peritoneal carcinomatosis during cytoreductive surgery [197], and, most recently, the evaluation of melanoma [135, 198]. An operating room compatible, mobile confocal microscope (Figure 8 A-D) has been used to directly observe patient tumor vasculature associated with primary or in-transit melanomas [199]. Consistent with preclinical observations, patient tumor vessels are disorganized and tortuous, and ~50% of them do not support blood flow. Human tumor vessel diameters are larger than those predicted from immunohistochemistry or preclinical IVM and thereby have lower wall shear stress, influencing drug delivery and cellular immunotherapies. Thus, real-time clinical imaging of living human superficial or endoluminal tumors may be helpful in monitoring local therapies [199].

PAI also has demonstrated great potentials in clinical tumor vascular imaging, especially in breast cancer. PAI with a hemispherical detector array has shown advantages in visualizing fine vasculature, detailed blood-vessel branching structures and morphological characteristics compared over MRI [200]. A single-breath-hold photoacoustic computed

tomography (SBH-PACT) system developed by Wang LV *et al.* features a deep penetration depth (4 cm) with high spatial and temporal resolutions (255 μm in-plane resolution and a 10 Hz 2D frame rate) (Figure 9) [74]. By scanning the entire breast within a single breath hold (~ 15 s), a volumetric image can be acquired and then is reconstructed utilizing 3D back-projection with negligible breath-induced motion artifacts, visualizing detailed angiographic structures in human breasts. SBH-PACT has

demonstrated an early promise in high sensitivity detection of breast cancers in radiographically dense breasts by detecting higher blood vessel densities in tumors than in normal breast tissue [74]. In addition, the high imaging speed of SBH-PACT enables dynamic studies, such as photoacoustic elastography, which identifies tumors by their reduced tissue compliance without resorting to ionizing radiation or exogenous contrast [74].

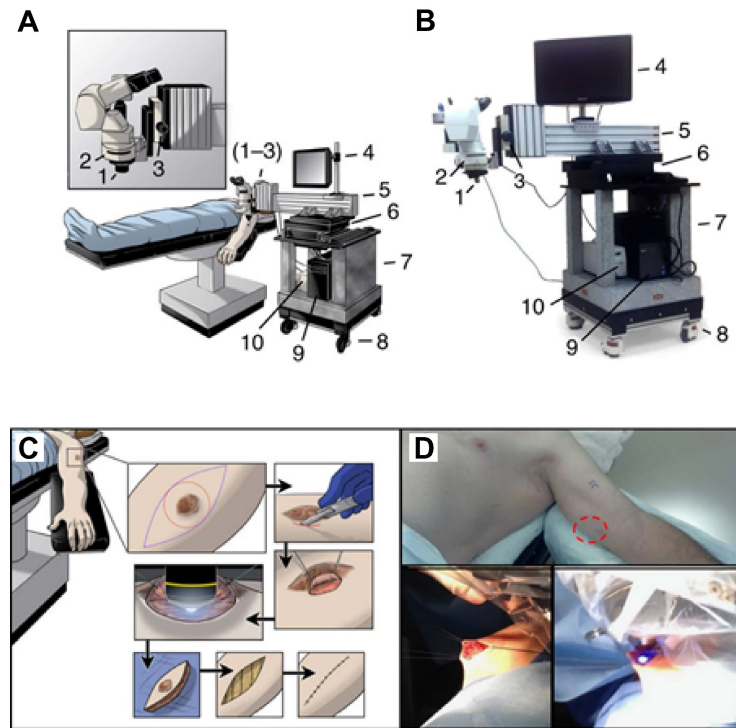


Figure 8. Clinical IVM. (A). Schematic and (B) photograph of the IVM unit designed as a mobile system for observations in the operating room. Critical systems allowing for stable epifluorescence observation of patient tumors in real-time are highlighted as follows: (1) $\times 10$ objective lens ($\times 100$ total including $\times 10$ subjective lens), (2) fluorescent filter cube, (3) fine focus knob, (4) monitor to observe in real time, (5) cantilevered arm to extend the system over the patient and hold the apparatus steady, (6) heavy movement platform to control fine x-y motion of the system during observation, (7) solid granite base to reduce vibrations, (8) locking wheels, allowing mobility and stability, (9) integrated computer system to record observations and store data and (10) fluorescent light source. (C) Schematic and (D) representative photographs, detailing the surgical procedure to examine tumor microvasculature. Briefly, an incision is made in the skin overlying or adjacent to the tumor (red circle) to allow access for direct tumor observation. The epifluorescent light source is activated and digital recording commences with real time observation of the intravenous injection of fluorescein. Following observation, the access site is closed, and a standard oncologic resection performed. Adapted from [199] with permission, 2016 Springer Nature.

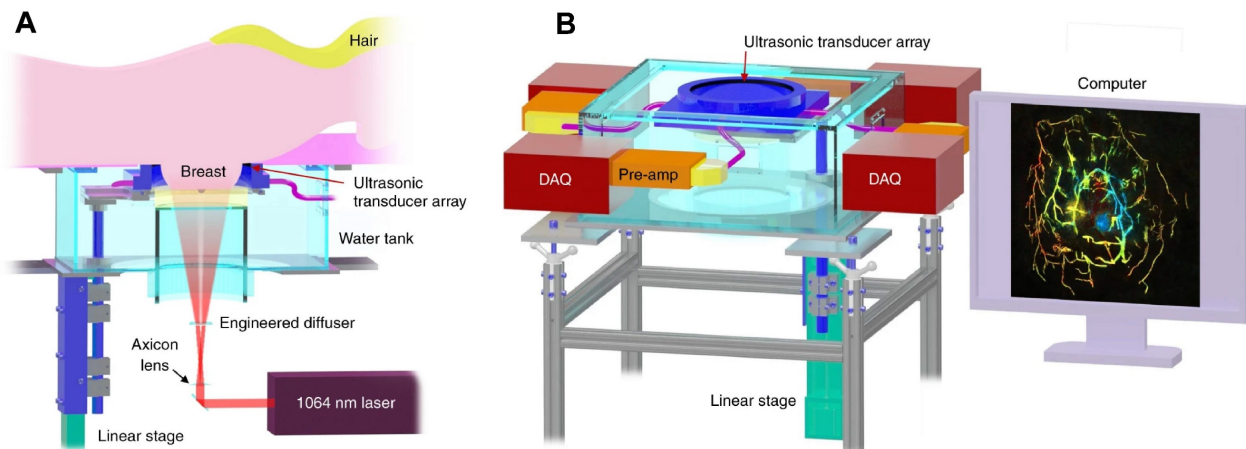


Figure 9. Clinical PAI. Representations of the SBH-PACT system. (A). Perspective cut-away view of the system with data acquisition components removed. (B). Perspective view of the system with patient bed and optical components removed. DAQ: data acquisition system, Pre-amp: pre-amplifier circuits. Adapted from [74] with permission, 2018 Springer Nature.

In order to expand clinical applications of intravital imaging, the development of customer-friendly intravital imaging platforms is essential. A portable wi-fi-enabled microscope could conceivably be combined with a smartphone or watch and would be very convenient for monitoring vasculature of superficial cancers reachable by laser light penetration (~2-4 cm), for conditions such as melanoma, oral cancers, and breast cancers. Light weight, multiple-color fluorescence imaging during endoscopy or cystoscopy could visualize blood vessels of gastrointestinal and bladder cancers. Additionally, intravital imaging would allow immediate diagnosis during a surgical operation and help the surgeon precisely excise the cancer tissue. To enable these advances, multi-disciplinary collaborations that bring surgeons and engineers together will be needed. Once sufficient clinical data are accumulated, artificial intelligence-based intravital imaging and analysis tools could be developed, which will help speed the analysis of blood vessels, diagnose, and grade cancers, and predict treatment responses.

In summary, recent advances in intravital imaging technologies, including label-free, multi-modality, and subcellular imaging, and non-invasive methods to visualize tumor vasculatures have a bright future in preclinical and clinical applications. These technical advances promise a diverse toolset with which the examination of tumor vasculature under various conditions, with or without therapies, can be performed. Observations from these studies would form the basis for the next generation of cancer therapies.

Supplementary Material

Supplementary table.

<https://www.thno.org/v13p5223s1.pdf>

Competing Interests

The authors have declared that no competing interest exists.

References

- Ruoslahti E. Specialization of tumour vasculature. *Nat Rev Cancer*. 2002; 2: 83-90.
- Minchinton AI, Tannock IF. Drug penetration in solid tumours. *Nat Rev Cancer*. 2006; 6: 583-92.
- De Palma M, Bizziato D, Petrova TV. Microenvironmental regulation of tumour angiogenesis. *Nat Rev Cancer*. 2017; 17: 457-74.
- Schaaf MB, Garg AD, Agostinis P. Defining the role of the tumor vasculature in antitumor immunity and immunotherapy. *Cell Death Dis*. 2018; 9: 115.
- McDonald DM, Choyke PL. Imaging of angiogenesis: from microscope to clinic. *Nat Med*. 2003; 9: 713-25.
- Morikawa S, Baluk P, Kaidoh T, Haskell A, Jain RK, McDonald DM. Abnormalities in pericytes on blood vessels and endothelial sprouts in tumors. *Am J Pathol*. 2002; 160: 985-1000.
- Claesson-Welsh L, Dejana E, McDonald DM. Permeability of the Endothelial Barrier: Identifying and Reconciling Controversies. *Trends Mol Med*. 2021; 27: 314-31.
- Konerding MA, Miodonski AJ, Lametschwandtner A. Microvascular corrosion casting in the study of tumor vascularity: a review. *Scanning Microsc*. 1995; 9: 1233-43.
- Wettschureck N, Strlic B, Offermanns S. Passing the Vascular Barrier: Endothelial Signaling Processes Controlling Extravasation. *Physiol Rev*. 2019; 99: 1467-525.
- de Lázaro I, Mooney DJ. A nanoparticle's pathway into tumours. *Nat Mater*. 2020; 19: 486-7.
- Sindhvani S, Syed AM, Ngai J, Kingston BR, Maiorino L, Rothschild J, et al. The entry of nanoparticles into solid tumours. *Nat Mater*. 2020; 19: 566-75.
- Carmeliet P, Jain RK. Principles and mechanisms of vessel normalization for cancer and other angiogenic diseases. *Nat Rev Drug Discov*. 2011; 10: 417-27.
- Hendry SA, Farnsworth RH, Solomon B, Achen MG, Stacker SA, Fox SB. The Role of the Tumor Vasculature in the Host Immune Response: Implications for Therapeutic Strategies Targeting the Tumor Microenvironment. *Front Immunol*. 2016; 7: 621.
- Munn LL, Jain RK. Vascular regulation of antitumor immunity. *Science*. 2019; 365: 544-5.
- Chouaib S, Noman MZ, Kosmatopoulos K, Curran MA. Hypoxic stress: obstacles and opportunities for innovative immunotherapy of cancer. *Oncogene*. 2017; 36: 439-45.
- Nakagawa Y, Negishi Y, Shimizu M, Takahashi M, Ichikawa M, Takahashi H. Effects of extracellular pH and hypoxia on the function and development of antigen-specific cytotoxic T lymphocytes. *Immunol Lett*. 2015; 167: 72-86.
- Azzi S, Hebda JK, Gavard J. Vascular permeability and drug delivery in cancers. *Front Oncol*. 2013; 3: 211.
- Hobbs SK, Monsky WL, Yuan F, Roberts WG, Griffith L, Torchilin VP, et al. Regulation of transport pathways in tumor vessels: role of tumor type and microenvironment. *Proc Natl Acad Sci U S A*. 1998; 95: 4607-12.
- Hashizume H, Baluk P, Morikawa S, McLean JW, Thurston G, Roberge S, et al. Openings between defective endothelial cells explain tumor vessel leakiness. *Am J Pathol*. 2000; 156: 1363-80.
- Tozer GM, Ameer-Beg SM, Baker J, Barber PR, Hill SA, Hodgkiss RJ, et al. Intravital imaging of tumour vascular networks using multi-photon fluorescence microscopy. *Adv Drug Deliv Rev*. 2005; 57: 135-52.
- Baluk P, Morikawa S, Haskell A, Mancuso M, McDonald DM. Abnormalities of basement membrane on blood vessels and endothelial sprouts in tumors. *Am J Pathol*. 2003; 163: 1801-15.
- Kiessling F, Greschus S, Lichy MP, Bock M, Fink C, Vosseler S, et al. Volumetric computed tomography (VCT): a new technology for noninvasive, high-resolution monitoring of tumor angiogenesis. *Nat Med*. 2004; 10: 1133-8.
- Christensen-Jeffries K, Couture O, Dayton PA, Eldar YC, Hynynen K, Kiessling F, et al. Super-resolution Ultrasound Imaging. *Ultrasound Med Biol*. 2020; 46: 865-91.
- Errico C, Pierre J, Pezet S, Desailly Y, Lenkei Z, Couture O, et al. Ultrafast ultrasound localization microscopy for deep super-resolution vascular imaging. *Nature*. 2015; 527: 499-502.
- Conchello JA, Lichtman JW. Optical sectioning microscopy. *Nat Methods*. 2005; 2: 920-31.
- Denk W, Strickler JH, Webb WW. Two-photon laser scanning fluorescence microscopy. *Science*. 1990; 248: 73-6.
- Weigert R, Porat-Shliom N, Amornphimoltham P. Imaging cell biology in live animals: ready for prime time. *J Cell Biol*. 2013; 201: 969-79.
- Schießl IM, Castrop H. Deep insights: intravital imaging with two-photon microscopy. *Pflugers Arch*. 2016; 468: 1505-16.
- Campagnola PJ, Loew LM. Second-harmonic imaging microscopy for visualizing biomolecular arrays in cells, tissues and organisms. *Nat Biotechnol*. 2003; 21: 1356-60.
- Débarre D, Supatto W, Pena AM, Fabre A, Tordjmann T, Combettes L, et al. Imaging lipid bodies in cells and tissues using third-harmonic generation microscopy. *Nat Methods*. 2006; 3: 47-53.
- Weigelin B, Bakker GJ, Friedl P. Third harmonic generation microscopy of cells and tissue organization. *J Cell Sci*. 2016; 129: 245-55.
- Maiti S, Shear JB, Williams RM, Zipfel WR, Webb WW. Measuring serotonin distribution in live cells with three-photon excitation. *Science*. 1997; 275: 530-2.
- Brown EB, Campbell RB, Tsuzuki Y, Xu L, Carmeliet P, Fukumura D, et al. In vivo measurement of gene expression, angiogenesis and physiological function in tumors using multiphoton laser scanning microscopy. *Nat Med*. 2001; 7: 864-8.
- Fukumura D, Jain RK. Imaging angiogenesis and the microenvironment. *Apmis*. 2008; 116: 695-715.
- You S, Tu H, Chaney EJ, Sun Y, Zhao Y, Bower AJ, et al. Intravital imaging by simultaneous label-free autofluorescence-multiharmonic microscopy. *Nat Commun*. 2018; 9: 2125.

36. Parpaleix A, Goulam Houssen Y, Charpak S. Imaging local neuronal activity by monitoring PO₂ transients in capillaries. *Nat Med.* 2013; 19: 241-6.
37. Lecoq J, Parpaleix A, Roussakis E, Ducros M, Goulam Houssen Y, Vinogradov SA, et al. Simultaneous two-photon imaging of oxygen and blood flow in deep cerebral vessels. *Nat Med.* 2011; 17: 893-8.
38. Tu H, Liu Y, Turchinovich D, Marjanovic M, Lyngsø J, Lægsgaard J, et al. Stain-free histopathology by programmable supercontinuum pulses. *Nat Photonics.* 2016; 10: 534-40.
39. Oreopoulos J, Berman R, Browne M. Spinning-disk confocal microscopy: present technology and future trends. *Methods Cell Biol.* 2014; 123: 153-75.
40. McAllister RG, Sisan DR, Urbach JS. Design and optimization of a high-speed, high-sensitivity, spinning disk confocal microscopy system. *J Biomed Opt.* 2008; 13: 054058.
41. Vladymyrov M, Abe J, Moalli F, Stein JV, Ariga A. Real-time tissue offset correction system for intravital multiphoton microscopy. *J Immunol Methods.* 2016; 438: 35-41.
42. Warren SC, Nobis M, Magenau A, Mohammed YH, Herrmann D, Moran J, et al. Removing physiological motion from intravital and clinical functional imaging data. *Elife.* 2018; 7.
43. Ji N. Adaptive optical fluorescence microscopy. *Nat Methods.* 2017; 14: 374-80.
44. Martinez AF, McCachren SS, 3rd, Lee M, Murphy HA, Zhu C, Crouch BT, et al. Metaboloptics: Visualization of the tumor functional landscape via metabolic and vascular imaging. *Sci Rep.* 2018; 8: 4171.
45. Karreman MA, Mercier L, Schieber NL, Solecki G, Allio G, Winkler F, et al. Fast and precise targeting of single tumor cells in vivo by multimodal correlative microscopy. *J Cell Sci.* 2016; 129: 444-56.
46. Stelzer EH, Strobl F, Chang B-J, Preusser F, Preibisch S, McDole K, et al. Light sheet fluorescence microscopy. *Nat Rev Methods Primers.* 2021; 1: 73.
47. Power RM, Huisken J. A guide to light-sheet fluorescence microscopy for multiscale imaging. *Nat Methods.* 2017; 14: 360-73.
48. Voleti V, Patel KB, Li W, Perez Campos C, Bharadwaj S, Yu H, et al. Real-time volumetric microscopy of in vivo dynamics and large-scale samples with SCAPE 2.0. *Nat Methods.* 2019; 16: 1054-62.
49. Almagro J, Messall HA, Zaw Thin M, van Rheenen J, Behrens A. Tissue clearing to examine tumour complexity in three dimensions. *Nat Rev Cancer.* 2021; 21: 718-30.
50. Lagerweij T, Dusoswa SA, Negrean A, Hendrikx EML, de Vries HE, Kole J, et al. Optical clearing and fluorescence deep-tissue imaging for 3D quantitative analysis of the brain tumor microenvironment. *Angiogenesis.* 2017; 20: 533-46.
51. Cuccarese MF, Dubach JM, Pfirsche C, Engblom C, Garris C, Miller MA, et al. Heterogeneity of macrophage infiltration and therapeutic response in lung carcinoma revealed by 3D organ imaging. *Nat Commun.* 2017; 8: 14293.
52. Wan Y, McDole K, Keller PJ. Light-Sheet Microscopy and Its Potential for Understanding Developmental Processes. *Annu Rev Cell Dev Biol.* 2019; 35: 655-81.
53. Liu TL, Upadhyayula S, Milkie DE, Singh V, Wang K, Swinburne IA, et al. Observing the cell in its native state: Imaging subcellular dynamics in multicellular organisms. *Science.* 2018; 360.
54. Wu J, Lu Z, Jiang D, Guo Y, Qiao H, Zhang Y, et al. Iterative tomography with digital adaptive optics permits hour-long intravital observation of 3D subcellular dynamics at millisecond scale. *Cell.* 2021; 184: 3318-32.e17.
55. Headley MB, Bins A, Nip A, Roberts EW, Looney MR, Gerard A, et al. Visualization of immediate immune responses to pioneer metastatic cells in the lung. *Nature.* 2016; 531: 513-7.
56. Hong G, Antaris AL, Dai H. Near-infrared fluorophores for biomedical imaging. *Nat Biomed Eng.* 2017; 1: 0010.
57. Welsher K, Liu Z, Sherlock SP, Robinson JT, Chen Z, Daranciang D, et al. A route to brightly fluorescent carbon nanotubes for near-infrared imaging in mice. *Nat Nanotechnol.* 2009; 4: 773-80.
58. Hong G, Lee JC, Robinson JT, Raaz U, Xie L, Huang NF, et al. Multifunctional in vivo vascular imaging using near-infrared II fluorescence. *Nat Med.* 2012; 18: 1841-6.
59. Bruns OT, Bischof TS, Harris DK, Franke D, Shi Y, Riedemann L, et al. Next-generation in vivo optical imaging with short-wave infrared quantum dots. *Nat Biomed Eng.* 2017; 1.
60. Fan Y, Wang P, Lu Y, Wang R, Zhou L, Zheng X, et al. Lifetime-engineered NIR-II nanoparticles unlock multiplexed in vivo imaging. *Nat Nanotechnol.* 2018; 13: 941-6.
61. Li B, Zhao M, Feng L, Dou C, Ding S, Zhou G, et al. Organic NIR-II molecule with long blood half-life for in vivo dynamic vascular imaging. *Nat Commun.* 2020; 11: 3102.
62. Antaris AL, Chen H, Diao S, Ma Z, Zhang Z, Zhu S, et al. A high quantum yield molecule-protein complex fluorophore for near-infrared II imaging. *Nat Commun.* 2017; 8: 15269.
63. Li Y, Cai Z, Liu S, Zhang H, Wong STH, Lam JWY, et al. Design of AIEgens for near-infrared IIb imaging through structural modulation at molecular and morphological levels. *Nat Commun.* 2020; 11: 1255.
64. Zubkovs V, Antonucci A, Schuergers N, Lambert B, Latini A, Ceccarelli R, et al. Spinning-disk confocal microscopy in the second near-infrared window (NIR-II). *Sci Rep.* 2018; 8: 13770.
65. Wang F, Wan H, Ma Z, Zhong Y, Sun Q, Tian Y, et al. Light-sheet microscopy in the near-infrared II window. *Nat Methods.* 2019; 16: 545-52.
66. Wang F, Ma Z, Zhong Y, Salazar F, Xu C, Ren F, et al. In vivo NIR-II structured-illumination light-sheet microscopy. *Proc Natl Acad Sci U S A.* 2021; 118.
67. Wang F, Ren F, Ma Z, Qu L, Gourgues R, Xu C, et al. In vivo non-invasive confocal fluorescence imaging beyond 1,700 nm using superconducting nanowire single-photon detectors. *Nat Nanotechnol.* 2022; 17: 653-60.
68. Kamoun WS, Chae SS, Lacorre DA, Tyrrell JA, Mitre M, Gillissen MA, et al. Simultaneous measurement of RBC velocity, flux, hematocrit and shear rate in vascular networks. *Nat Methods.* 2010; 7: 655-60.
69. Honkura N, Richards M, Laviña B, Sáinz-Jaspeado M, Betsholtz C, Claesson-Welsh L. Intravital imaging-based analysis tools for vessel identification and assessment of concurrent dynamic vascular events. *Nat Commun.* 2018; 9: 2746.
70. Bernabeu MO, Köry J, Grogan JA, Markelc B, Beardo A, d'Avezac M, et al. Abnormal morphology biases hematocrit distribution in tumor vasculature and contributes to heterogeneity in tissue oxygenation. *Proc Natl Acad Sci U S A.* 2020; 117: 27811-9.
71. Enjalbert R, Hardman D, Krüger T, Bernabeu MO. Compressed vessels bias red blood cell partitioning at bifurcations in a hematocrit-dependent manner: Implications in tumor blood flow. *Proc Natl Acad Sci U S A.* 2021; 118.
72. Wang LV, Yao J. A practical guide to photoacoustic tomography in the life sciences. *Nat Methods.* 2016; 13: 627-38.
73. Wang LV, Hu S. Photoacoustic tomography: in vivo imaging from organelles to organs. *Science.* 2012; 335: 1458-62.
74. Lin L, Hu P, Shi J, Appleton CM, Maslov K, Li L, et al. Single-breath-hold photoacoustic computed tomography of the breast. *Nat Commun.* 2018; 9: 2352.
75. Liu C, Liang Y, Wang L. Single-shot photoacoustic microscopy of hemoglobin concentration, oxygen saturation, and blood flow in sub-microseconds. *Photoacoustics.* 2020; 17: 100156.
76. Li Y, Li L, Zhu L, Maslov K, Shi J, Hu P, et al. Snapshot Photoacoustic Tomography Through an Ergodic Relay for High-throughput Imaging of Optical Absorption. *Nat Photonics.* 2020; 14: 164-70.
77. Tzoumas S, Nunes A, Olefir I, Stangl S, Symvoulidis P, Glasl S, et al. Eigenspectra photoacoustic tomography achieves quantitative blood oxygenation imaging deep in tissues. *Nat Commun.* 2016; 7: 12121.
78. Lin Q, Deng D, Song X, Dai B, Yang X, Luo Q, et al. Self-Assembled "Off/On" Nanopomegranate for In Vivo Photoacoustic and Fluorescence Imaging: Strategic Arrangement of Kupffer Cells in Mouse Hepatic Lobules. *ACS Nano.* 2019; 13: 1526-37.
79. Song W, Xu Q, Zhang Y, Zhan Y, Zheng W, Song L. Fully integrated reflection-mode photoacoustic, two-photon, and second harmonic generation microscopy in vivo. *Sci Rep.* 2016; 6: 32240.
80. Lavaud J, Henry M, Coll JL, Jossier V. Exploration of melanoma metastases in mice brains using endogenous contrast photoacoustic imaging. *Int J Pharm.* 2017; 532: 704-9.
81. Quiros-Gonzalez I, Tomaszewski MR, Aitken SJ, Ansel-Bollepalli L, McDuffus LA, Gill M, et al. Photoacoustics delineates murine breast cancer models displaying angiogenesis and vascular mimicry. *Br J Cancer.* 2018; 118: 1098-106.
82. Chekkoury A, Nunes A, Gateau J, Symvoulidis P, Feuchtinger A, Beziere N, et al. High-Resolution Multispectral Photoacoustic Tomography of the Vascularization and Constitutive Hypoxemia of Cancerous Tumors. *Neoplasia.* 2016; 18: 459-67.
83. Bendinger AL, Glowa C, Peter J, Karger CP. Photoacoustic imaging to assess pixel-based sO₂ distributions in experimental prostate tumors. *J Biomed Opt.* 2018; 23: 1-11.
84. Tomaszewski MR, Gonzalez IQ, O'Connor JP, Abeyakoon O, Parker GJ, Williams KJ, et al. Oxygen Enhanced Photoacoustic Tomography (OE-OT) Reveals Vascular Dynamics in Murine Models of Prostate Cancer. *Theranostics.* 2017; 7: 2900-13.
85. Jathoul AP, Laufer J, Ogunlade O, Treeby B, Cox B, Zhang E, et al. Deep in vivo photoacoustic imaging of mammalian tissues using a tyrosinase-based genetic reporter. *Nat Photonics.* 2015; 9: 239-46.

86. Wang X, Zhang L, Wang J, Liu X, Lv P, Zeng J, et al. Size-Controlled Biocompatible Silver Nanoplates for Contrast-Enhanced Intravital Photoacoustic Mapping of Tumor Vasculature. *J Biomed Nanotechnol.* 2018; 14: 1448-57.
87. de Boer JF, Leitgeb R, Wojtkowski M. Twenty-five years of optical coherence tomography: the paradigm shift in sensitivity and speed provided by Fourier domain OCT [Invited]. *Biomed Opt Express.* 2017; 8: 3248-80.
88. Huang D, Swanson EA, Lin CP, Schuman JS, Stinson WG, Chang W, et al. Optical coherence tomography. *Science.* 1991; 254: 1178-81.
89. Vakoc BJ, Fukumura D, Jain RK, Bouma BE. Cancer imaging by optical coherence tomography: preclinical progress and clinical potential. *Nat Rev Cancer.* 2012; 12: 363-8.
90. Vakoc BJ, Lanning RM, Tyrrell JA, Padera TP, Bartlett LA, Stylianopoulos T, et al. Three-dimensional microscopy of the tumor microenvironment in vivo using optical frequency domain imaging. *Nat Med.* 2009; 15: 1219-23.
91. Welzel J, Schuh S, De Carvalho N, Themstrup L, Ulrich M, Jemec GBE, et al. Dynamic optical coherence tomography shows characteristic alterations of blood vessels in malignant melanoma. *J Eur Acad Dermatol Venereol.* 2021; 35: 1087-93.
92. Zhou N, Xu X, Liu Y, Wei W, Peng X. Appearance of Tumor Vessels in Patients With Choroidal Osteoma Using Swept-Source Optical Coherence Tomographic Angiography. *Front Oncol.* 2021; 11: 762394.
93. Chen D, Yuan W, Park HC, Li X. In vivo assessment of vascular-targeted photodynamic therapy effects on tumor microvasculature using ultrahigh-resolution functional optical coherence tomography. *Biomed Opt Express.* 2020; 11: 4316-25.
94. Wu S, Okada R, Liu Y, Fang Y, Yan F, Wang C, et al. Quantitative analysis of vascular changes during photoimmunotherapy using speckle variance optical coherence tomography (SV-OCT). *Biomed Opt Express.* 2021; 12: 1804-20.
95. Yashin K, Bonsanto MM, Achkasova K, Zolotova A, Wael AM, Kiseleva E, et al. OCT-Guided Surgery for Gliomas: Current Concept and Future Perspectives. *Diagnostics (Basel).* 2022; 12.
96. Si P, Honkala A, de la Zerda A, Smith BR. Optical Microscopy and Coherence Tomography of Cancer in Living Subjects. *Trends Cancer.* 2020; 6: 205-22.
97. Zopf LM, Heimel P, Geyer SH, Kavirayani A, Reier S, Fröhlich V, et al. Cross-Modality Imaging of Murine Tumor Vasculature—a Feasibility Study. *Mol Imaging Biol.* 2021; 23: 874-93.
98. Miller MJ, Wei SH, Parker I, Cahalan MD. Two-photon imaging of lymphocyte motility and antigen response in intact lymph node. *Science.* 2002; 296: 1869-73.
99. Stoll S, Delon J, Brotz TM, Germain RN. Dynamic imaging of T cell-dendritic cell interactions in lymph nodes. *Science.* 2002; 296: 1873-6.
100. Palmer GM, Fontanella AN, Shan S, Hanna G, Zhang G, Fraser CL, et al. In vivo optical molecular imaging and analysis in mice using dorsal window chamber models applied to hypoxia, vasculature and fluorescent reporters. *Nat Protoc.* 2011; 6: 1355-66.
101. Maeda A, DaCosta RS. Optimization of the dorsal skinfold window chamber model and multi-parametric characterization of tumor-associated vasculature. *Intravital.* 2014; 3: e27935.
102. Seynhaeve ALB, Ten Hagen TLM. An adapted dorsal skinfold model used for 4D intravital followed by whole-mount imaging to reveal endothelial cell-pericyte association. *Sci Rep.* 2021; 11: 20389.
103. Sobolik T, Su YJ, Ashby W, Schaffer DK, Wells S, Wikswo JP, et al. Development of novel murine mammary imaging windows to examine wound healing effects on leukocyte trafficking in mammary tumors with intravital imaging. *Intravital.* 2016; 5: e1125562.
104. Schafer R, Leung HM, Gmitro AF. Multi-modality imaging of a murine mammary window chamber for breast cancer research. *Biotechniques.* 2014; 57: 45-50.
105. Erten A, Wrasidlo W, Scadeng M, Esener S, Hoffman RM, Bouvet M, et al. Magnetic resonance and fluorescence imaging of doxorubicin-loaded nanoparticles using a novel in vivo model. *Nanomedicine.* 2010; 6: 797-807.
106. Jacquemin G, Benavente-Diaz M, Djaber S, Bore A, Dangles-Marie V, Surdez D, et al. Longitudinal high-resolution imaging through a flexible intravital imaging window. *Sci Adv.* 2021; 7.
107. Tsukada Y, Muramatsu F, Hayashi Y, Inagaki C, Su H, Iba T, et al. An in vivo model allowing continuous observation of human vascular formation in the same animal over time. *Sci Rep.* 2021; 11: 745.
108. Sipkins DA, Wei X, Wu JW, Runnels JM, Côté D, Means TK, et al. In vivo imaging of specialized bone marrow endothelial microdomains for tumour engraftment. *Nature.* 2005; 435: 969-73.
109. Hawkins ED, Duarte D, Akinduro O, Khorshed RA, Passaro D, Nowicka M, et al. T-cell acute leukaemia exhibits dynamic interactions with bone marrow microenvironments. *Nature.* 2016; 538: 518-22.
110. Chen Y, Maeda A, Bu J, DaCosta R. Femur Window Chamber Model for In Vivo Cell Tracking in the Murine Bone Marrow. *J Vis Exp.* 2016.
111. Reismann D, Stefanowski J, Günther R, Rakhymzhan A, Matthys R, Nützi R, et al. Longitudinal intravital imaging of the femoral bone marrow reveals plasticity within marrow vasculature. *Nat Commun.* 2017; 8: 2153.
112. Cramer SW, Carter RE, Aronson JD, Kodandaramaiah SB, Ebner TJ, Chen CC. Through the looking glass: A review of cranial window technology for optical access to the brain. *J Neurosci Methods.* 2021; 354: 109100.
113. Askoxylakis V, Badeaux M, Roberge S, Batista A, Kirkpatrick N, Snuderl M, et al. A cerebellar window for intravital imaging of normal and disease states in mice. *Nat Protoc.* 2017; 12: 2251-62.
114. Nia HT, Datta M, Seano G, Zhang S, Ho WW, Roberge S, et al. In vivo compression and imaging in mouse brain to measure the effects of solid stress. *Nat Protoc.* 2020; 15: 2321-40.
115. Looney MR, Thornton EE, Sen D, Lamm WJ, Glenn RW, Krummel MF. Stabilized imaging of immune surveillance in the mouse lung. *Nat Methods.* 2011; 8: 91-6.
116. Entenberg D, Rodriguez-Tirado C, Kato Y, Kitamura T, Pollard JW, Condeelis J. In vivo subcellular resolution optical imaging in the lung reveals early metastatic proliferation and motility. *Intravital.* 2015; 4: 1-11.
117. Entenberg D, Voiculescu S, Guo P, Borriello L, Wang Y, Karagiannis GS, et al. A permanent window for the murine lung enables high-resolution imaging of cancer metastasis. *Nat Methods.* 2018; 15: 73-80.
118. Marques PE, Antunes MM, David BA, Pereira RV, Teixeira MM, Menezes GB. Imaging liver biology in vivo using conventional confocal microscopy. *Nat Protoc.* 2015; 10: 258-68.
119. Babes L, Kubes P. Visualizing the Tumor Microenvironment of Liver Metastasis by Spinning Disk Confocal Microscopy. *Methods Mol Biol.* 2016; 1458: 203-15.
120. Ritsma L, Steller EJ, Ellenbroek SI, Kranenburg O, Borel Rinkes IH, van Rheeën J. Surgical implantation of an abdominal imaging window for intravital microscopy. *Nat Protoc.* 2013; 8: 583-94.
121. Ritsma L, Steller EJ, Beerling E, Loomans CJ, Zomer A, Gerlach C, et al. Intravital microscopy through an abdominal imaging window reveals a pre-micrometastasis stage during liver metastasis. *Sci Transl Med.* 2012; 4: 158ra45.
122. Martins AF, Clavijo Jordan V, Bochner F, Chirayil S, Paranawithana N, Zhang S, et al. Imaging Insulin Secretion from Mouse Pancreas by MRI Is Improved by Use of a Zinc-Responsive MRI Sensor with Lower Affinity for Zn(2+) Ions. *J Am Chem Soc.* 2018; 140: 17456-64.
123. Bochner F, Mohan V, Zinger A, Golani O, Schroeder A, Sagi I, et al. Intravital imaging of vascular anomalies and extracellular matrix remodeling in orthotopic pancreatic tumors. *Int J Cancer.* 2020; 146: 2209-17.
124. Bochner F, Fellus-Alyagor L, Kalchenko V, Shinar S, Neeman M. A Novel Intravital Imaging Window for Longitudinal Microscopy of the Mouse Ovary. *Sci Rep.* 2015; 5: 12446.
125. Huang Q, Cohen MA, Alsina FC, Devlin G, Garrett A, McKey J, et al. Intravital imaging of mouse embryos. *Science.* 2020; 368: 181-6.
126. Li Y, Song Y, Zhao L, Gaidosh G, Latties AM, Wen R. Direct labeling and visualization of blood vessels with lipophilic carbocyanine dye DiI. *Nat Protoc.* 2008; 3: 1703-8.
127. Neri D, Bicknell R. Tumour vascular targeting. *Nat Rev Cancer.* 2005; 5: 436-46.
128. Lui BG, Salomon N, Wüsthube-Lausch J, Daneschdar M, Schmoltdt HU, Türeci Ö, et al. Targeting the tumor vasculature with engineered cystine-knot miniproteins. *Nat Commun.* 2020; 11: 295.
129. Ng TSC, Garlin MA, Weissleder R, Miller MA. Improving nanotherapy delivery and action through image-guided systems pharmacology. *Theranostics.* 2020; 10: 968-97.
130. Lin Q, Fathi P, Chen X. Nanoparticle delivery in vivo: A fresh look from intravital imaging. *EBioMedicine.* 2020; 59: 102958.
131. Lu L, Sun Y, Wan C, Hu Y, Lo PC, Lovell JF, et al. Role of intravital imaging in nanomedicine-assisted anti-cancer therapy. *Curr Opin Biotechnol.* 2021; 69: 153-61.
132. Wang Z. Imaging Nanotherapeutics in Inflamed Vasculature by Intravital Microscopy. *Theranostics.* 2016; 6: 2431-8.
133. Miller MA, Weissleder R. Imaging of anticancer drug action in single cells. *Nat Rev Cancer.* 2017; 17: 399-414.
134. Fukumura D, Duda DG, Munn LL, Jain RK. Tumor microvasculature and microenvironment: novel insights through intravital imaging in pre-clinical models. *Microcirculation.* 2010; 17: 206-25.
135. Gabriel EM, Fisher DT, Evans S, Takabe K, Skitzki JJ. Intravital microscopy in the study of the tumor microenvironment: from bench to human application. *Oncotarget.* 2018; 9: 20165-78.

136. Nakasone ES, Askautrud HA, Kees T, Park JH, Plaks V, Ewald AJ, et al. Imaging tumor-stroma interactions during chemotherapy reveals contributions of the microenvironment to resistance. *Cancer Cell*. 2012; 21: 488-503.
137. Harney AS, Arwert EN, Entenberg D, Wang Y, Guo P, Qian BZ, et al. Real-Time Imaging Reveals Local, Transient Vascular Permeability, and Tumor Cell Intravasation Stimulated by TIE2hi Macrophage-Derived VEGFA. *Cancer Discov*. 2015; 5: 932-43.
138. Karagiannis GS, Pastoriza JM, Wang Y, Harney AS, Entenberg D, Pignatelli J, et al. Neoadjuvant chemotherapy induces breast cancer metastasis through a TMEM-mediated mechanism. *Sci Transl Med*. 2017; 9.
139. Matsumoto Y, Nichols JW, Toh K, Nomoto T, Cabral H, Miura Y, et al. Vascular bursts enhance permeability of tumour blood vessels and improve nanoparticle delivery. *Nat Nanotechnol*. 2016; 11: 533-8.
140. Peng F, Setyawati MI, Tee JK, Ding X, Wang J, Nga ME, et al. Nanoparticles promote in vivo breast cancer cell intravasation and extravasation by inducing endothelial leakiness. *Nat Nanotechnol*. 2019; 14: 279-86.
141. Inoue Y, Matsumoto Y, Toh K, Miyano K, Cabral H, Igarashi K, et al. Manipulating dynamic tumor vessel permeability to enhance polymeric micelle accumulation. *J Control Release*. 2021; 329: 63-75.
142. Li S, Zhang Y, Wang J, Zhao Y, Ji T, Zhao X, et al. Nanoparticle-mediated local depletion of tumour-associated platelets disrupts vascular barriers and augments drug accumulation in tumours. *Nat Biomed Eng*. 2017; 1: 667-79.
143. Mehta D, Malik AB. Signaling mechanisms regulating endothelial permeability. *Physiol Rev*. 2006; 86: 279-367.
144. Zhou Q, Shao S, Wang J, Xu C, Xiang J, Piao Y, et al. Enzyme-activatable polymer-drug conjugate augments tumour penetration and treatment efficacy. *Nat Nanotechnol*. 2019; 14: 799-809.
145. Chen S, Zhong Y, Fan W, Xiang J, Wang G, Zhou Q, et al. Enhanced tumour penetration and prolonged circulation in blood of polyzwitterion-drug conjugates with cell-membrane affinity. *Nat Biomed Eng*. 2021; 5: 1019-27.
146. Passaro D, Di Tullio A, Abarrategi A, Rouault-Pierre K, Foster K, Ariza-McNaughton L, et al. Increased Vascular Permeability in the Bone Marrow Microenvironment Contributes to Disease Progression and Drug Response in Acute Myeloid Leukemia. *Cancer Cell*. 2017; 32: 324-41.e6.
147. Pirillo C, Birch F, Tissot FS, Anton SG, Haltalli M, Tini V, et al. Metalloproteinase inhibition reduces AML growth, prevents stem cell loss, and improves chemotherapy effectiveness. *Blood Adv*. 2022; 6: 3126-41.
148. Yin H, Frontini MJ, Arpino JM, Nong Z, O'Neil C, Xu Y, et al. Fibroblast Growth Factor 9 Imparts Hierarchy and Vasoreactivity to the Microcirculation of Renal Tumors and Suppresses Metastases. *J Biol Chem*. 2015; 290: 22127-42.
149. Kesler CT, Pereira ER, Cui CH, Nelson GM, Masuck DJ, Baish JW, et al. Angiopoietin-4 increases permeability of blood vessels and promotes lymphatic dilation. *Faseb j*. 2015; 29: 3668-77.
150. Uhl C, Markel M, Broggin T, Nieminen M, Kremenetskaia I, Vajkoczy P, et al. EphB4 mediates resistance to antiangiogenic therapy in experimental glioma. *Angiogenesis*. 2018; 21: 873-81.
151. Miller MA, Chandra R, Cuccarese MF, Pfirschke C, Engblom C, Stapleton S, et al. Radiation therapy primes tumors for nanotherapeutic delivery via macrophage-mediated vascular bursts. *Sci Transl Med*. 2017; 9.
152. Kammertoens T, Friese C, Arina A, Idel C, Briesemeister D, Rothe M, et al. Tumour ischaemia by interferon- γ resembles physiological blood vessel regression. *Nature*. 2017; 545: 98-102.
153. Frontini MJ, Nong Z, Gros R, Drangova M, O'Neil C, Rahman MN, et al. Fibroblast growth factor 9 delivery during angiogenesis produces durable, vasoreactive microvessels wrapped by smooth muscle cells. *Nat Biotechnol*. 2011; 29: 421-7.
154. Melnikov PA, Valikhov MP, Kuznetsov, II, Grinenko NF, Sukhinich KK, Simbirtsev AS, et al. Analysis of the Effect of IL-1 β on Blood-Brain Barrier Permeability in M6 Glioma Mouse Model Using Intravital Microscopy. *Bull Exp Biol Med*. 2019; 168: 118-24.
155. Dolmans DE, Kadambi A, Hill JS, Waters CA, Robinson BC, Walker JP, et al. Vascular accumulation of a novel photosensitizer, MV6401, causes selective thrombosis in tumor vessels after photodynamic therapy. *Cancer Res*. 2002; 62: 2151-6.
156. He C, Agharkar P, Chen B. Intravital microscopic analysis of vascular perfusion and macromolecule extravasation after photodynamic vascular targeting therapy. *Pharm Res*. 2008; 25: 1873-80.
157. Chen B, Pogue BW, Luna JM, Hardman RL, Hoopes PJ, Hasan T. Tumor vascular permeabilization by vascular-targeting photosensitization: effects, mechanism, and therapeutic implications. *Clin Cancer Res*. 2006; 12: 917-23.
158. Zhen Z, Tang W, Chuang YJ, Todd T, Zhang W, Lin X, et al. Tumor vasculature targeted photodynamic therapy for enhanced delivery of nanoparticles. *ACS Nano*. 2014; 8: 6004-13.
159. Huis In 't Veld RV, Ritsma L, Kleinovink JW, Que I, Ossendorp F, Cruz LJ. Photodynamic cancer therapy enhances accumulation of nanoparticles in tumor-associated myeloid cells. *J Control Release*. 2020; 320: 19-31.
160. Kobayashi H, Choyke PL. Super enhanced permeability and retention (SUPR) effects in tumors following near infrared photoimmunotherapy. *Nanoscale*. 2016; 8: 12504-9.
161. Stapleton S, Jaffray D, Milosevic M. Radiation effects on the tumor microenvironment: Implications for nanomedicine delivery. *Adv Drug Deliv Rev*. 2017; 109: 119-30.
162. Zhu L, Yu X, Wang L, Liu J, Qu Z, Zhang H, et al. Angiogenesis and immune checkpoint dual blockade in combination with radiotherapy for treatment of solid cancers: opportunities and challenges. *Oncogenesis*. 2021; 10: 47.
163. Barker HE, Paget JT, Khan AA, Harrington KJ. The tumour microenvironment after radiotherapy: mechanisms of resistance and recurrence. *Nat Rev Cancer*. 2015; 15: 409-25.
164. Castle KD, Kirsch DG. Establishing the Impact of Vascular Damage on Tumor Response to High-Dose Radiation Therapy. *Cancer Res*. 2019; 79: 5685-92.
165. Garcia-Barros M, Paris F, Cordon-Cardo C, Lyden D, Rafii S, Haimovitz-Friedman A, et al. Tumor response to radiotherapy regulated by endothelial cell apoptosis. *Science*. 2003; 300: 1155-9.
166. Rodríguez-Barbeito P, Díaz-Botana P, Gago-Arias A, Feijoo M, Neira S, Guiu-Souto J, et al. A Model of Indirect Cell Death Caused by Tumor Vascular Damage after High-Dose Radiotherapy. *Cancer Res*. 2019; 79: 6044-53.
167. Wang HH, Cui YL, Zaorsky NG, Lan J, Deng L, Zeng XL, et al. Mesenchymal stem cells generate pericytes to promote tumor recurrence via vasculogenesis after stereotactic body radiation therapy. *Cancer Lett*. 2016; 375: 349-59.
168. Kioi M, Vogel H, Schultz G, Hoffman RM, Harsh GR, Brown JM. Inhibition of vasculogenesis, but not angiogenesis, prevents the recurrence of glioblastoma after irradiation in mice. *J Clin Invest*. 2010; 120: 694-705.
169. Sonveaux P, Brouet A, Havaux X, Grégoire V, Dessy C, Balligand JL, et al. Irradiation-induced angiogenesis through the up-regulation of the nitric oxide pathway: implications for tumor radiotherapy. *Cancer Res*. 2003; 63: 1012-9.
170. Kleibeker EA, Fokas E, Allen PD, Kersemans V, Griffioen AW, Beech J, et al. Low dose angiostatic treatment counteracts radiotherapy-induced tumor perfusion and enhances the anti-tumor effect. *Oncotarget*. 2016; 7: 76613-27.
171. Allam N, Jeffrey Zabel W, Demidov V, Jones B, Fluerau C, Taylor E, et al. Longitudinal in-vivo quantification of tumour microvascular heterogeneity by optical coherence angiography in pre-clinical radiation therapy. *Sci Rep*. 2022; 12: 6140.
172. Couzin-Frankel J. Breakthrough of the year 2013. *Cancer immunotherapy*. *Science*. 2013; 342: 1432-3.
173. Zhang Y, Zhang Z. The history and advances in cancer immunotherapy: understanding the characteristics of tumor-infiltrating immune cells and their therapeutic implications. *Cell Mol Immunol*. 2020; 17: 807-21.
174. Waldman AD, Fritz JM, Lenardo MJ. A guide to cancer immunotherapy: from T cell basic science to clinical practice. *Nat Rev Immunol*. 2020; 20: 651-68.
175. Sahu M, Suryawanshi H. Immunotherapy: The future of cancer treatment. *J Oral Maxillofac Pathol*. 2021; 25: 371.
176. Balar AV, Weber JS. PD-1 and PD-L1 antibodies in cancer: current status and future directions. *Cancer Immunol Immunother*. 2017; 66: 551-64.
177. Arlauckas SP, Garris CS, Kohler RH, Kitaoka M, Cuccarese MF, Yang KS, et al. In vivo imaging reveals a tumor-associated macrophage-mediated resistance pathway in anti-PD-1 therapy. *Sci Transl Med*. 2017; 9.
178. Berraondo P, Sanmamed MF, Ochoa MC, Etxeberria I, Aznar MA, Pérez-Gracia JL, et al. Cytokines in clinical cancer immunotherapy. *Br J Cancer*. 2019; 120: 6-15.
179. Huang Y, Goel S, Duda DG, Fukumura D, Jain RK. Vascular normalization as an emerging strategy to enhance cancer immunotherapy. *Cancer Res*. 2013; 73: 2943-8.
180. Yi M, Jiao D, Qin S, Chu Q, Wu K, Li A. Synergistic effect of immune checkpoint blockade and anti-angiogenesis in cancer treatment. *Mol Cancer*. 2019; 18: 60.
181. Lee WS, Yang H, Chon HJ, Kim C. Combination of anti-angiogenic therapy and immune checkpoint blockade normalizes vascular-immune crosstalk to potentiate cancer immunity. *Exp Mol Med*. 2020; 52: 1475-85.

182. Lanitis E, Irving M, Coukos G. Targeting the tumor vasculature to enhance T cell activity. *Curr Opin Immunol.* 2015; 33: 55-63.
183. Arina A, Beckett M, Fernandez C, Zheng W, Pitroda S, Chmura SJ, et al. Tumor-reprogrammed resident T cells resist radiation to control tumors. *Nat Commun.* 2019; 10: 3959.
184. Murty S, Haile ST, Beinat C, Aalipour A, Alam IS, Murty T, et al. Intravital imaging reveals synergistic effect of CAR T-cells and radiation therapy in a preclinical immunocompetent glioblastoma model. *Oncoimmunology.* 2020; 9: 1757360.
185. Cramer GM, Cengel KA, Busch TM. Forging Forward in Photodynamic Therapy. *Cancer Res.* 2022; 82: 534-6.
186. Acker G, Palumbo A, Neri D, Vajkoczy P, Czabanka M. F8-SIP mediated targeted photodynamic therapy leads to microvascular dysfunction and reduced glioma growth. *J Neurooncol.* 2016; 129: 33-8.
187. de Bruijn HS, Mashayekhi V, Schreurs TJJ, van Driel P, Strijkers GJ, van Diest PJ, et al. Acute cellular and vascular responses to photodynamic therapy using EGFR-targeted nanobody-photosensitizer conjugates studied with intravital optical imaging and magnetic resonance imaging. *Theranostics.* 2020; 10: 2436-52.
188. Haedicke K, Agemy L, Omar M, Bereznoi A, Roberts S, Longo-Machado C, et al. High-resolution optoacoustic imaging of tissue responses to vascular-targeted therapies. *Nat Biomed Eng.* 2020; 4: 286-97.
189. Liu Y, Bhattarai P, Dai Z, Chen X. Photothermal therapy and photoacoustic imaging via nanotheranostics in fighting cancer. *Chem Soc Rev.* 2019; 48: 2053-108.
190. Day ES, Zhang L, Thompson PA, Zawaski JA, Kaffes CC, Gaber MW, et al. Vascular-targeted photothermal therapy of an orthotopic murine glioma model. *Nanomedicine (Lond).* 2012; 7: 1133-48.
191. Liang CP, Nakajima T, Watanabe R, Sato K, Choyke PL, Chen Y, et al. Real-time monitoring of hemodynamic changes in tumor vessels during photodynamic therapy using optical coherence tomography. *J Biomed Opt.* 2014; 19: 98004.
192. Kiesslich R, Gossner L, Goetz M, Dahlmann A, Vieth M, Stolte M, et al. In vivo histology of Barrett's esophagus and associated neoplasia by confocal laser endomicroscopy. *Clin Gastroenterol Hepatol.* 2006; 4: 979-87.
193. Wallace MB, Meining A, Canto MI, Fockens P, Miehlke S, Roesch T, et al. The safety of intravenous fluorescein for confocal laser endomicroscopy in the gastrointestinal tract. *Aliment Pharmacol Ther.* 2010; 31: 548-52.
194. Nakao M, Yoshida S, Tanaka S, Takemura Y, Oka S, Yoshihara M, et al. Optical biopsy of early gastroesophageal cancer by catheter-based reflectance-type laser-scanning confocal microscopy. *J Biomed Opt.* 2008; 13: 054043.
195. Xie XJ, Li CQ, Zuo XL, Yu T, Gu XM, Li Z, et al. Differentiation of colonic polyps by confocal laser endomicroscopy. *Endoscopy.* 2011; 43: 87-93.
196. Wu K, Liu JJ, Adams W, Sonn GA, Mach KE, Pan Y, et al. Dynamic real-time microscopy of the urinary tract using confocal laser endomicroscopy. *Urology.* 2011; 78: 225-31.
197. Gabriel EM, Kim M, Fisher DT, Mangum C, Attwood K, Ji W, et al. A pilot trial of intravital microscopy in the study of the tumor vasculature of patients with peritoneal carcinomatosis. *Sci Rep.* 2021; 11: 4946.
198. Gabriel EM, Kim M, Fisher DT, Powers C, Attwood K, Bagaria SP, et al. Dynamic control of tumor vasculature improves antitumor responses in a regional model of melanoma. *Sci Rep.* 2020; 10: 13245.
199. Fisher DT, Muhitch JB, Kim M, Doyen KC, Bogner PN, Evans SS, et al. Intraoperative intravital microscopy permits the study of human tumour vessels. *Nat Commun.* 2016; 7: 10684.
200. Toi M, Asao Y, Matsumoto Y, Sekiguchi H, Yoshikawa A, Takada M, et al. Visualization of tumor-related blood vessels in human breast by photoacoustic imaging system with a hemispherical detector array. *Sci Rep.* 2017; 7: 41970.